Band mixing and particle-hole asymmetry in moiré fractional Chern insulators

Nicolás Morales-Durán,[1,*] Jingtian Shi,[2] Cristian Voinea,[3,1] Paweł Potasz,[4] and Jennifer Cano[5,1]

[1]*Center for Computational Quantum Physics, Flatiron Institute, New York, New York 10010, USA*
[2]*Materials Science Division, Argonne National Laboratory, Lemont, Illinois 60439, USA*
[3]*School of Physics and Astronomy, University of Leeds, Leeds LS2 9JT, United Kingdom*
[4]*Institute of Physics, Faculty of Physics, Astronomy and Informatics, Nicolaus Copernicus University, Grudziadzka 5, 87-100 Toruń, Poland*
[5]*Department of Physics and Astronomy, Stony Brook University, Stony Brook, New York 11794, USA*

(Received 7 May 2026; accepted 27 October 2026; published 9 November 2026)

We investigate the effect of remote band mixing on the stability of fractional Chern insulators in a family of models that approximate continuum descriptions of moiré materials. Our results suggest that the experimentally observed asymmetry between filling fractions $\nu = 1/3$ and $\nu = 2/3$ in twisted $MoTe_2$ originates from a competition between a fractional Chern insulator, an electron Wigner crystal, and a hole Wigner crystal. In the absence of band mixing, the leading instability at $\nu = 1/3$ is the electron crystal, whereas at $\nu = 2/3$ the main competing phase is the hole crystal. Remote band mixing substantially lowers the energy of the electron crystal but has only a weak effect on the hole crystal. Consequently, it brings competing crystalline states much closer in energy to the fractional Chern insulator at $\nu = 1/3$ than at $\nu = 2/3$, leading to a stronger suppression of the many-body gap. This mechanism also provides an explanation for the emergence of reentrant integer quantum anomalous Hall states in moiré $MoTe_2$ for fillings $\nu > 1/2$.

DOI: 10.1103/zf45-1gvb

I. INTRODUCTION

The phase diagram of moiré twisted $MoTe_2$ ($tMoTe_2$) has been characterized through a combination of transport, optical, and orbital magnetization measurements [1–24], revealing an extraordinary diversity of correlated electronic states as a function of electron density, displacement field, and twist angle. Most strikingly, fractionally filling the topmost moiré valence band of $tMoTe_2$ led to the first observation of fractional quantum anomalous Hall (FQAH) states, also known as fractional Chern insulators (FCIs) [25–29]. Alongside these developments, reentrant integer quantum anomalous Hall (RIQAH) states, anomalous Hall metals, and signatures of unconventional superconductivity have also been observed [10].

Although the FQAH phases are expected to be adiabatically connected to their counterparts in the lowest Landau level (LLL), experiments in $tMoTe_2$ reveal striking departures from the behavior of conventional two-dimensional electron gases in strong magnetic fields. Notably, the correlated topological phases in $tMoTe_2$ are strongest at filling fractions $\nu > 1/2$, with the $\nu = 2/3$ FQAH state emerging as the most prominent, followed by the state at $\nu = 3/5$. In contrast, the $\nu = 1/3$ state—typically the most robust in the LLL—was observed only very recently [16], and earlier experiments instead reported a trivial correlated insulator at the same filling fraction. These differences raise fundamental questions about the origin and stability of correlated phases in moiré systems.

A substantial body of recent theoretical and numerical work has explored the nature of FQAH ground states in moiré materials and their competition with other correlated phases. Owing to the exponential growth of the Hilbert space, however, most exact diagonalization (ED) [30–35] and density matrix renormalization group (DMRG) [36,37] studies are restricted to a single isolated band. These studies typically find FCI ground states at both $\nu = 1/3$ and $\nu = 2/3$, albeit with different many-body gaps, consistent with the absence of particle-hole symmetry in bands with a nonuniform quantum metric [38,39], and in contrast to the LLL. However, these single-band approaches systematically predict robust FCI states on both sides of $\nu = 1/2$, in disagreement with the experimental observations.

A natural source of this discrepancy is the role of remote bands. Remote band mixing becomes significant when the band gap is comparable to the interaction strength, which is the case across much of the $tMoTe_2$ phase diagram. Multiband ED studies of continuum moiré models [40–43] show that including remote bands and the valley degree of freedom destabilizes the FCI state at $\nu = 1/3$, favoring the relative robustness of the $\nu = 2/3$ phase, in closer agreement with experiment. This picture is further supported by recent large-scale approaches, including DMRG [44], neural quantum state variational Monte Carlo (VMC) [45,46], and similarity renormalization group methods [47], which incorporate band mixing and access larger system sizes. These studies consistently find that while band mixing weakens FCI states in

*Contact author: nmoralesduran@flatironinstitute.org

Published by the American Physical Society under the terms of the Creative Commons Attribution 4.0 International license. Further distribution of this work must maintain attribution to the author(s) and the published article's title, journal citation, and DOI.

favor of competing charge density wave (CDW) order at both fillings, the FCI remains significantly more stable at $\nu = 2/3$ than at $\nu = 1/3$. Despite this growing numerical consensus, the microscopic mechanism by which band mixing preferentially stabilizes FQAH phases at $\nu > 1/2$ in semiconductor moiré systems such as $tMoTe_2$ remains unclear.

In this work, we propose that remote band mixing provides a microscopic mechanism for the pronounced particle-hole asymmetry observed in semiconductor moiré materials by preferentially stabilizing electron Wigner crystals over hole Wigner crystals. Our central result is that remote band mixing destabilizes the $\nu = 1/3$ fractional state more strongly than the $\nu = 2/3$ state because it lowers the energy of competing electron Wigner crystal states more efficiently than that of hole Wigner crystal states, thereby reducing the excitation gap even while the many-body ground state remains in the fractional quantum Hall (FQH)-like phase throughout most of the parameter regime we study. To test this hypothesis, we perform exact diagonalization studies of the many-body ground states and low-lying excitation spectra of a family of Hamiltonians that form a controlled hierarchy of approximations to continuum models of semiconductor moiré materials [48,49]. Specifically, we investigate the evolution of the fractional quantum Hall/fractional Chern insulator states at fillings $\nu = 1/3$ and $\nu = 2/3$ as the strength of remote band mixing is increased, considering in turn Landau levels, Aharonov-Casher (AC) bands [50], and adiabatic bands [48,49]. This unified approach allows us to disentangle two distinct sources of particle-hole asymmetry about $\nu = 1/2$: nonuniform Berry curvature of the active band and the effects of remote band mixing.

The response of the many-body gap to Landau level (LL) mixing differs qualitatively between the two fillings: While the FCI gap at $\nu = 1/3$ decreases monotonically with increasing band mixing, the gap at $\nu = 2/3$ exhibits a nonmonotonic evolution, initially increasing before eventually declining. We trace this behavior to a shift in the wave vector of the magnetoroton minimum, which manifests as a level crossing between low-lying excited states in the many-body spectrum. We argue that this level crossing reflects a competition between electron and hole Wigner crystal instabilities, providing a natural explanation for the enhanced robustness of the $\nu = 2/3$ state across a broad parameter regime. We further show that this mechanism remains operative in the presence of nonuniform Berry curvature and finite bandwidth. Finally, we connect our results to prior numerical studies of continuum descriptions of $tMoTe_2$, offering a microscopic explanation for the pronounced particle-hole asymmetry observed experimentally.

II. MANY-BODY HAMILTONIANS

We now describe the Hamiltonian for all three models studied here. The single-particle Hamiltonian is that of a Schrödinger particle of mass m^* subject to a periodic magnetic field $B(\boldsymbol{r})$ and a periodic potential $U(\boldsymbol{r})$, namely,

$$H_0 = \frac{1}{2m^*}\Pi_-\Pi_+ + U(\boldsymbol{r}), \tag{1}$$

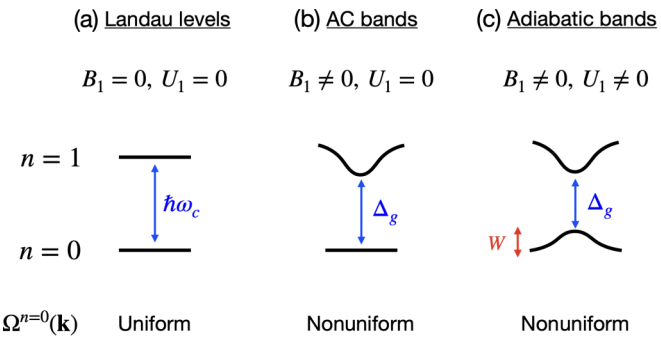


FIG. 1. Schematics of the different single-particle models considered in this work. (a) In Landau levels ($B_1 = U_1 = 0$), all bands are flat with uniform quantum geometry, which is ideal in the LLL. (b) In the AC model ($B_1 \neq 0, U_1 = 0$), the lowest band is flat and has (nonuniform) ideal quantum geometry, while the first remote band is dispersive. (c) In the adiabatic model ($B_1, U_1 \neq 0$), all bands are dispersive and the quantum geometry is not ideal. We project interactions to the $n = 0$ and $n = 1$ bands and obtain the ground state by the ED method. We denote the gap between the two noninteracting bands as Δ_g, which for Landau levels is just the cyclotron gap $\hbar\omega_c$; the bandwidth of the $n = 0$ adiabatic band is W and $\Omega^{n=0}$ is the Berry curvature of the lowest band.

with kinetic-momentum operators given by

$$\Pi_\pm = [p_x + A_x(\boldsymbol{r})] \pm i[p_y + A_y(\boldsymbol{r})], \tag{2}$$

where $p_\alpha = -i\partial_\alpha$ for $\alpha = x, y$. The magnetic field can be split into its average and periodic parts,

$$B(\boldsymbol{r}) = \nabla \times \boldsymbol{A}(\boldsymbol{r}) = B_0 + \delta B(\boldsymbol{r}). \tag{3}$$

We take $B(\boldsymbol{r})$ and $U(\boldsymbol{r})$ to form triangular lattices with lattice constant a_M, and adopt the convention that the magnetic field has one flux quantum per unit cell. This relates a_M to the magnetic length of the average magnetic field, $\ell^2 = \hbar/eB_0$, by $\ell^2 = (\sqrt{3}/4\pi)\, a_M^2$.

The continuum model of a single valley of $tMoTe_2$ is recovered by choosing $B(\boldsymbol{r})$ and $U(\boldsymbol{r})$ according to the parametrization of Refs. [48,49] for a given twist angle, so that varying the twist angle traces out a path in the parameter space of $B(\boldsymbol{r})$ and $U(\boldsymbol{r})$. In the following, we assume valley polarization, which is consistent with recent experiments reporting a valley-polarized ground state in $tMoTe_2$ at both $\nu = 1/3$ and $\nu = 2/3$ [16].

To be concrete, we truncate the periodic functions at their first harmonic (the first-star approximation),

$$\delta B(\boldsymbol{r}) = \sum_{\boldsymbol{G}} B_1\, e^{i\boldsymbol{G}\cdot\boldsymbol{r}} \quad \text{and} \quad U(\boldsymbol{r}) = \sum_{\boldsymbol{G}} U_1\, e^{i\boldsymbol{G}\cdot\boldsymbol{r}}, \tag{4}$$

where $\boldsymbol{G}$ are the reciprocal lattice vectors of smallest magnitude. We take B_1 to have units of ℓ^{-2}; U_1 has units of energy, $e^2/\varepsilon\ell$, where ε is the dielectric constant. The different models we study are obtained by choosing different values for B_1 and U_1: the LL Hamiltonian has $B_1 = U_1 = 0$; the AC Hamiltonian has $B_1 \neq 0, U_1 = 0$; and the adiabatic Hamiltonian has both B_1 and U_1 nonzero; this distinction and consequences for the band structure and quantum geometry are summarized in Fig. 1. Further details on how the adiabatic Hamiltonian in Eq. (1) approximates the continuum model for twisted

homobilayer TMDs can be found in Appendix A, and in Refs. [49,51].

Electronic interactions are projected into the two lowest bands of Eq. (1), so that the many-body Hamiltonian is

$$H = \sum_{\boldsymbol{k},n} \epsilon_{n,\boldsymbol{k}}\, c^{\dagger}_{\boldsymbol{k},n} c_{\boldsymbol{k},n} + \frac{1}{2} \sum_{i,j,k,l} V^{n_i n_j n_k n_l}_{\boldsymbol{k}_i \boldsymbol{k}_j \boldsymbol{k}_k \boldsymbol{k}_l}\, c^{\dagger}_{n_i,\boldsymbol{k}_i} c^{\dagger}_{n_j,\boldsymbol{k}_j} c_{n_l,\boldsymbol{k}_l} c_{n_k,\boldsymbol{k}_k}, \tag{5}$$

where $\epsilon_{n,\boldsymbol{k}}$ is a single-particle energy, $c^{\dagger}_{n,\boldsymbol{k}}$ creates a particle in band n with momentum $\boldsymbol{k}$, and the interaction matrix elements are

$$V^{n_i n_j n_k n_l}_{\boldsymbol{k}_i \boldsymbol{k}_j \boldsymbol{k}_k \boldsymbol{k}_l} = \langle n_i, \boldsymbol{k}_i\,; n_j, \boldsymbol{k}_j | V | n_k, \boldsymbol{k}_k\,; n_l, \boldsymbol{k}_l \rangle\,, \tag{6}$$

where $|n, \boldsymbol{k}\rangle$ are the Bloch states of Eq. (1). The single-particle energies and eigenstates of Eq. (1) are obtained by diagonalizing the Hamiltonian in the basis of the Landau levels of the average magnetic field B_0, using the Coulomb gauge for the vector potential [49]. We obtain the many-body ground state of the interacting Hamiltonian in Eq. (5) using ED. For the calculations presented in the main text, we will use the unscreened Coulomb interaction $V(\boldsymbol{q}) = 2\pi e^2/\varepsilon \boldsymbol{q}$. In realistic systems, screening effects are relevant. For that reason, in Appendix B we present additional results for interactions corresponding to the first Haldane pseudopotential, $V(\boldsymbol{q}) = -V_1 \boldsymbol{q}^2$ and to a screened Coulomb interaction due to metallic gates at distance d, $V(\boldsymbol{q}) = 2\pi e^2 \tanh(qd)/\varepsilon \boldsymbol{q}$. The results for the three types of interactions display the same qualitative behavior.

The many-body spectrum is determined by three energy scales: the interaction strength $e^2/\varepsilon\ell$; the gap Δ_g between the two bands in the Hilbert space; and the bandwidth W of the lowest band. The band mixing is largely controlled by the ratio of the first two energy scales, $\kappa \equiv (e^2/\varepsilon\ell)/\Delta_g$. To isolate the effect of band mixing on the ground state, we have fixed the band gap Δ_g and tuned the dielectric constant ε. We study the effect of κ on the many-body gap; since the FCI ground state is characterized by a threefold quasidegeneracy on the finite torus [29], we define the many-body gap as $\Delta = \varepsilon_4 - \varepsilon_3$, where ε_n is the energy of the nth many-body eigenstate.

The calculations presented in the main text were performed on a system with $N = 12$ moiré unit cells and periodic boundary conditions corresponding to the Brillouin zone discretization shown in Fig. 2(a). In Appendix B, we present additional results for other system sizes and boundary conditions, as well as for the sphere geometry. Our results are consistent across all geometries and system sizes considered.

III. LANDAU LEVELS

We start by taking $B_1 = U_1 = 0$ in Eq. (1), which corresponds to the $n = 0$ and $n = 1$ LLs. The quantum geometry of the bands is uniform and satisfies $\mathrm{Tr}\, g_{\boldsymbol{k}} = (2n+1)\,\Omega_{\boldsymbol{k}}$, where $g_{\boldsymbol{k}}$ is the quantum metric, $\Omega_{\boldsymbol{k}}$ is the Berry curvature, and n is the LL index. The many-body physics is controlled entirely by the ratio between the interaction energy and the cyclotron gap, namely, $\kappa = (e^2/\varepsilon\ell)/(\hbar\omega_c)$. LL mixing plays a central role in the first ($n = 1$) LL, where it strongly influences

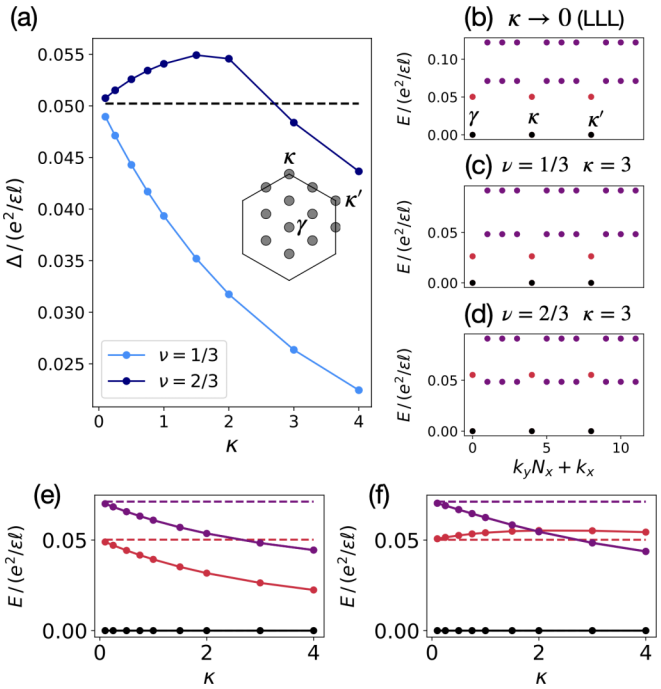


FIG. 2. Exact diagonalization results for Landau levels. (a) One-band-projected (dashed line) and two-band-projected (lines with dots) many-body gaps for fillings $\nu = 1/3,\ 2/3$ as a function of LL mixing; the FQH ground state persists even for $\kappa \gg 1$. Inset indicates the geometry used for ED calculations. (b) Many-body spectrum for LLL-projected calculations; particle-hole symmetry requires the spectra for $\nu = 1/3$ and $\nu = 2/3$ be identical. (c), (d) Many-body spectra for two-band-projected calculations with $\kappa = 3$ at $\nu = 1/3$ and $\nu = 2/3$, respectively. (e), (f) Evolution of the low-energy states as a function of κ for filling fractions $\nu = 1/3$ and $\nu = 2/3$, respectively. Dashed lines correspond to single-band-projected calculations and solid lines to two-band-projected calculations. The states in red correspond to the $\boldsymbol{\gamma}, \boldsymbol{\kappa}, \boldsymbol{\kappa}'$ points and the states in purple to the other nine momentum sectors. At $\nu = 2/3$, the two lowest excitations cross, giving rise to the nonmonotonic behavior in the many-body gap in panel (a).

the competition between the Pfaffian and anti-Pfaffian states at half-filling [52–58]. In contrast, in the LLL ($n = 0$), LL mixing has a more limited impact. For Abelian fractional quantum Hall states such as those at fillings $\nu = 1/3$ and $\nu = 2/3$, it does not change the ground state (indeed, these states remain robust even at $\kappa \gg 1$ [59–62]), but LL mixing can renormalize the gap and energy spectrum.

Our ED calculations systematically track the behavior of the many-body gap at filling fractions $\nu = 1/3$ and $2/3$ as a function of LL mixing, revealing trends and differences between the two fillings that extend to the lattice systems we study in subsequent sections. Before analyzing the results, we emphasize that the many-body gap remains positive over the parameter range studied, indicating that the FQH state remains the ground state even for large values of κ. However, we interpret a decreasing many-body gap as increasing energetic competitiveness of crystalline states.

We now describe our results. In Fig. 2(a), we show the one-band-projected and two-band-projected many-body gaps at $\nu = 1/3$ and $\nu = 2/3$, as a function of κ. The two gaps

coincide for calculations projected to the $n = 0$ band, as required by the particle-hole symmetry of the LLL. They also coincide in the limit $\kappa \to 0$, which effectively corresponds to an LLL projection and whose spectrum is shown in Fig. 2(b). However, generically, the two-band-projected many-body gaps are different at the two fillings, and, furthermore, exhibit different trends: While at $\nu = 1/3$, the gap decreases monotonically with LL mixing [59], the gap at $\nu = 2/3$ displays nonmonotonic behavior as a function of κ. This change in the magnitude of the gap is accompanied by a change in the many-body spectrum: While the fractional quantum Hall ground state survives over the entire range of κ considered, strong LL mixing qualitatively alters the excitation spectrum at $\nu = 2/3$, shifting the lowest-energy excitation to a different momentum sector. To demonstrate that this is not a finite-size or geometry-dependent effect, in Appendix B we show ED results for different torus geometries with $N = 12$ and $N = 15$ unit cells, along with ED calculations on the sphere geometry. We consistently recover the nonmonotonic behavior for the many-body gap at $\nu = 2/3$.

We now discuss the many-body spectra in detail. Typical many-body ED spectra at finite κ are shown in Fig. 2(c) at $\nu = 1/3$ and Fig. 2(d) at $\nu = 2/3$. Both display threefold quasidegenerate ground states at $\boldsymbol{\gamma}, \boldsymbol{\kappa}, \boldsymbol{\kappa}'$, along with many excited states. For two-band calculations, the lowest excited states at $\nu = 1/3$ are also at the $\boldsymbol{\gamma}, \boldsymbol{\kappa}, \boldsymbol{\kappa}'$ points, for all values of κ. In contrast, at $\nu = 2/3$ the lowest excited states shift from $\boldsymbol{\gamma}, \boldsymbol{\kappa}, \boldsymbol{\kappa}'$ to the other nine momentum points at a critical value of κ, whose specific value depends on system size and geometry. In Figs. 2(e) and 2(f), we show the evolution of the low-lying many-body energy levels with respect to the ground state as a function of κ, for filling fractions $\nu = 1/3$ and $\nu = 2/3$, respectively. The nonmonotonic behavior of the many-body gap at $\nu = 2/3$ is due to a level crossing between two excited states, which, as we will discuss, reflects a shift in the wave vector of the magnetoroton minimum. For completeness, in Appendix B we also present ED results in the limit where the $n = 0$ and $n = 1$ LLs are degenerate, which applies to the zeroth LL of bilayer graphene. Our results coincide with previous studies [63,64] showing that the gap at $\nu = 2/3$ is larger than the gap at $\nu = 1/3$, in agreement with experimental observations [65–67].

The lowest-energy excited state in the ED spectra—the magnetoroton minimum [68]—occurs at a wave vector set by the lattice constant of a competing CDW state. In the context of LLs, the lowest-energy CDW state at $\nu = 1/3$ is an electron Wigner crystal, while the most competitive CDW at $\nu = 2/3$ is a hole Wigner crystal [69]. Both states have a periodicity $a_c = (4\pi\sqrt{3})^{1/2}\,\ell = \sqrt{3}\,a_M$, corresponding to a wave vector that coincides with the $\boldsymbol{\kappa}, \boldsymbol{\kappa}'$ points of the Brillouin zone in our calculations. The electron crystal is topologically trivial, with Chern number $C = 0$, while the hole crystal has $C = 1$ and is an example of a partial Hall crystal [70,71]. Other competing states (which are higher in energy in the absence of band mixing [69]) are the hole crystal at $\nu = 1/3$ and the electron crystal at $\nu = 2/3$. These two states share the periodicity $a_c = \sqrt{3/2}\,a_M$, which is incommensurate with the periodicity of the fields $B(\boldsymbol{r})$ and $U(\boldsymbol{r})$ included in later sections; consequently, their reciprocal lattice vectors do not coincide with any of the Brillouin zone points in our calculations. The charge density in all four states is schematically shown in Figs. 3(a)–3(d).

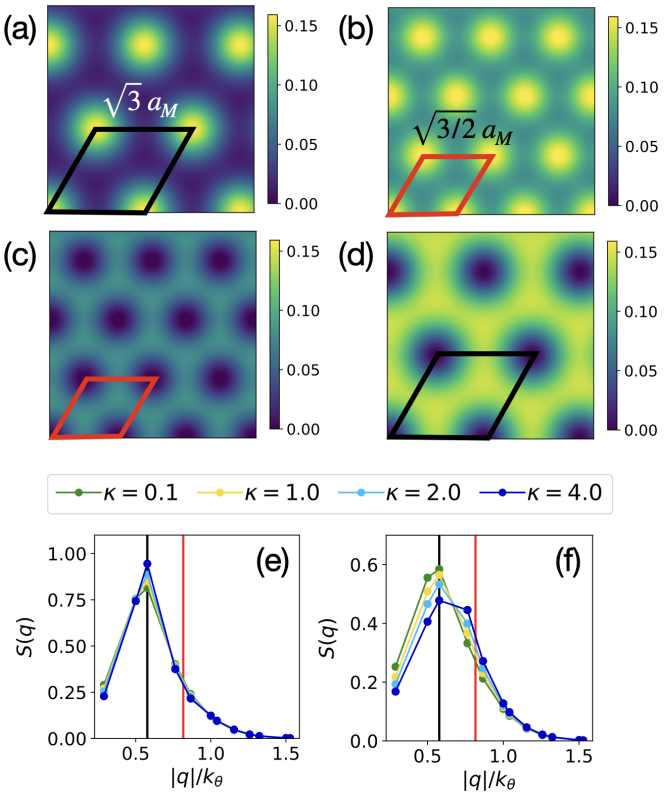


FIG. 3. Charge densities of the Wigner crystals competing with the fractional quantum Hall states. (a), (b) Electron crystals at $\nu = 1/3$ and $\nu = 2/3$, respectively. (c), (d) Hole crystals at $\nu = 1/3$ and $\nu = 2/3$, respectively. The unit cells and lattice constants are indicated. The periodicity $a_c = \sqrt{3}\,a_M$ is commensurate with that of $B(\boldsymbol{r})$. For $\nu = 1/3$, the electron crystal has lower energy, while for $\nu = 2/3$ the hole crystal has lower energy [69]. (e), (f) Structure factor of the two-band-projected FQH ground state for several values of κ. The vertical lines indicate the wave vectors corresponding to the phase with periodicity $\sqrt{3}\,a_M$ (black) and $\sqrt{3/2}\,a_M$ (red). Momentum is measured in units of $k_\theta = 4\pi/\sqrt{3}a_M$.

In Figs. 3(e) and 3(f), we show the FQH ground-state structure factor $S(\boldsymbol{q}) = \langle \rho_{\boldsymbol{q}} \rho_{-\boldsymbol{q}} \rangle / N_e$, where N_e is the number of particles and $\rho_{\boldsymbol{q}}$ is the band-projected density [72], for different values of κ at $\nu = 1/3$ and $\nu = 2/3$. We observe a peak at the $\boldsymbol{\kappa}, \boldsymbol{\kappa}'$ points for $\nu = 1/3$, which slightly grows in magnitude with LL mixing. In contrast, for $\nu = 2/3$ the main peak in the structure factor is at $\boldsymbol{\kappa}, \boldsymbol{\kappa}'$ for small κ and a second peak, which eventually dominates, starts to form at a larger wave vector for large κ. This is consistent with the many-body spectrum on the sphere, where, as a function of angular momentum, the magnetoroton minimum shifts to larger wave vectors with increasing LL mixing (see Appendix B for details).

LL mixing is known to lower the energy of electron Wigner crystals more strongly than that of their hole counterparts [73,74]. We therefore interpret the level crossing at $\nu = 2/3$ as a signature of a change in the dominant CDW instability: At small κ, the leading instability is toward a hole Wigner crystal with periodicity $a_c = \sqrt{3}\,a_M$, but as κ increases, LL mixing

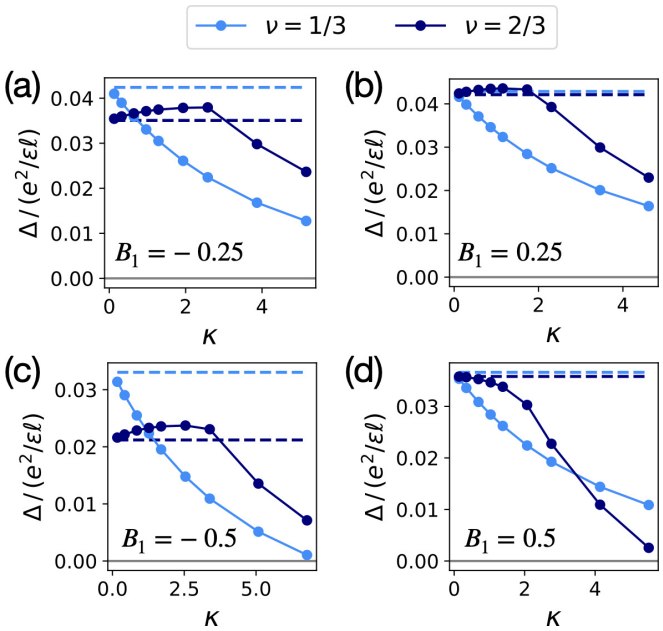


FIG. 4. Exact diagonalization results for AC bands with different values of B_1, as indicated. The Brillouin zone geometry is the same as in Fig. 2. One-band-projected (dashed line) and two-band-projected (lines with dots) many-body gaps for fillings $\nu = 1/3,\ 2/3$ as a function of band mixing. Due to the nonuniform quantum geometry of the $n = 0$ band, the gap at $\nu = 1/3$ exceeds that at $\nu = 2/3$ for one-band-projected calculations. Band mixing, however, can reverse this ordering.

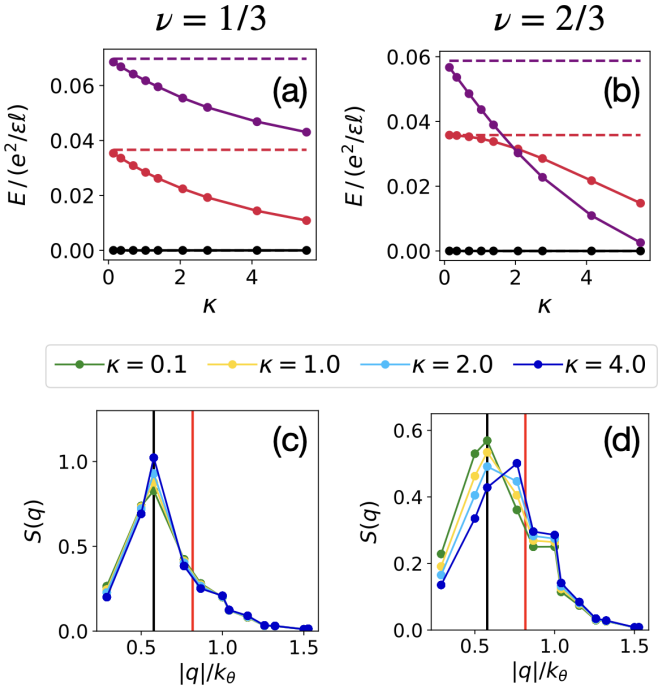


FIG. 5. Evolution of the low-energy many-body states as a function of κ at (a) $\nu = 1/3$ and (b) $\nu = 2/3$ for an AC band with $B_1 = 0.5$. Dashed lines correspond to single-band-projected calculations and lines with dots to two-band-projected calculations. The color convention is the same as for Fig. 2. Ground-state structure factors at (c) $\nu = 1/3$ and (d) $\nu = 2/3$ for several values of κ. The vertical lines indicate the wave vectors corresponding to the crystal unit cells shown in Fig. 3. The level crossing in panel (b) correlates with the shift in the main peak of $S(q)$ in panel (d). Note that a secondary peak develops at the first shell of reciprocal lattice vectors $|q| = k_\theta$.

progressively stabilizes the electron crystal with periodicity $a_c = \sqrt{3/2}\, a_M$. This transition naturally explains the observed shift of the magnetoroton minimum to larger wave vectors.

In the following sections, we show that the qualitative dependence of the FQH many-body gaps at $\nu = 1/3$ and $\nu = 2/3$ on LL mixing persists in both the AC and adiabatic models.

IV. AHARONOV-CASHER BANDS

We now turn to the AC band, where the magnetic field $B(\boldsymbol{r})$ in Eq. (1) is spatially modulated, but the potential $U(\boldsymbol{r})$ is absent. For concreteness, we keep only the first harmonic B_1 of the magnetic field, as described in Eq. (4). As illustrated in Fig. 1, the $n = 0$ band is flat and ideal, but has nonuniform Berry curvature, while the $n = 1$ band is dispersive and its quantum geometry is not equal to that of the $n = 1$ LL. Due to the nonuniform Berry curvature, particle-hole symmetry is broken at the one-band-projected level, while due to the remote band dispersion, the band gap Δ_g is smaller than the cyclotron gap in the limit $B_1 = 0$. Hence, we define the band-mixing parameter as $\kappa \equiv (e^2/\varepsilon\ell)/\Delta_g$. As we will show, our calculations of the many-body spectrum disentangle the effects of quantum geometry and remote band mixing on the particle-hole asymmetry.

Figure 4 shows the behavior of the many-body gaps at fillings $\nu = 1/3$ and $\nu = 2/3$ for AC bands with different values of B_1 as a function of the band-mixing parameter κ. The single-band-projected gaps (dashed lines) remain constant, although they no longer coincide with each other due to the particle-hole asymmetry introduced by the nonuniform quantum geometry [38,39]. For the $N = 12$ geometry considered here, the particle-hole asymmetry is noticeable for $B_1 < 0$ and almost vanishing for $B_1 > 0$. In Appendix B, we show similar ED results for different boundary conditions and system sizes, which indicate that the particle-hole asymmetry coming from the quantum metric of the $n = 0$ AC band depends significantly on the momentum discretization for small systems, and that this dependence becomes less severe as the system size is increased. Nonetheless, we consistently observe that the many-body gap at $\nu = 1/3$ is larger than at $\nu = 2/3$ for all calculations projected onto the $n = 0$ AC band. Single-band-projected ED studies of continuum models of $tMoTe_2$ [30,32–35] observe that the two gaps have similar magnitudes, suggesting that the quantum geometry of the topmost band alone is insufficient to explain the experimental particle-hole asymmetry, which favors the FCI at $\nu = 2/3$.

The effect of band mixing with the $n = 1$ AC band induces an additional particle-hole asymmetry above and below $\nu = 1/2$, as can be seen from the two-band-projected many-body gaps in Fig. 4 (lines with dots). The gap at $\nu = 1/3$ decreases monotonically as a function of κ for all values of B_1, while the gap at $\nu = 2/3$ displays a behavior similar to the one observed for Landau levels. In Figs. 5(a) and 5(b), we show

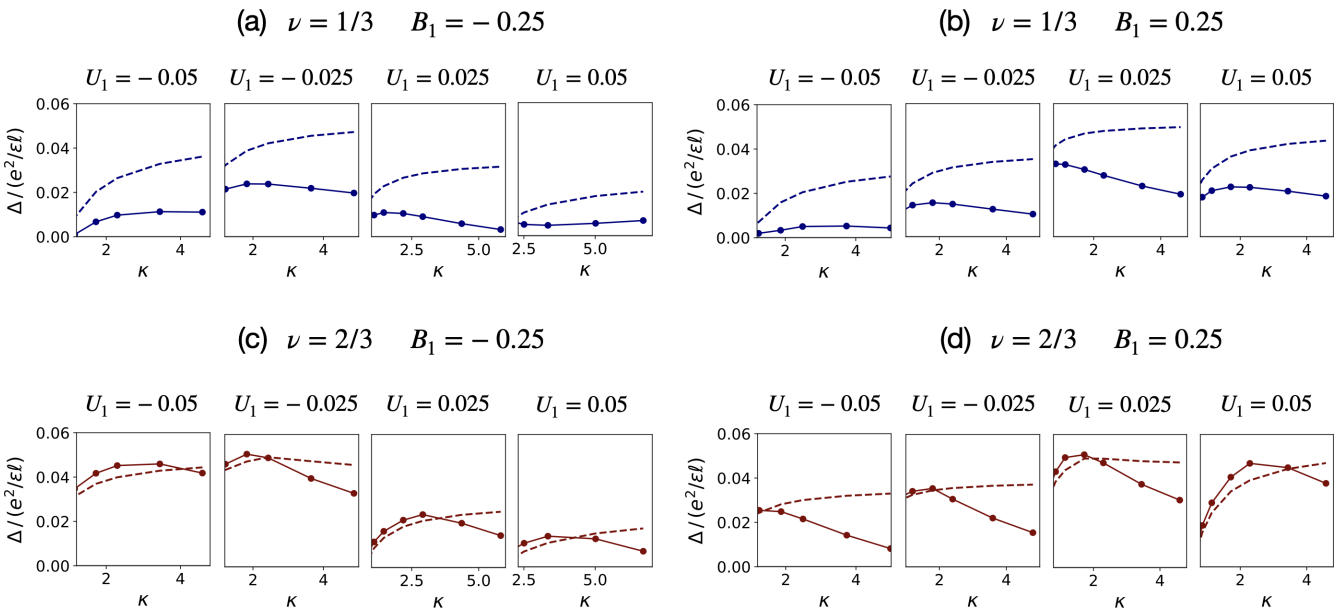


FIG. 6. Exact diagonalization results for adiabatic bands. Evolution of the many-body gaps as a function of κ for different adiabatic bands at filling fractions (a), (b) $\nu = 1/3$ and (c), (d) $\nu = 2/3$. We have fixed $B_1 \neq 0$ in all calculations and vary U_1 as indicated in each panel. Dashed lines and lines with dots are one-band- and two-band-projected calculations, respectively. The one-band-projected gaps increase with κ and asymptote to a constant value in the limit $e^2/\varepsilon\ell \gg W$ (equivalently as $\kappa \to \infty$).

the evolution of the lowest many-body energy levels with κ for an AC band with $B_1 = 0.5$ and for both filling fractions $\nu = 1/3$ and $\nu = 2/3$, respectively. There is a level crossing at $\nu = 2/3$, which explains why the many-body gap behaves different than its counterpart at $\nu = 1/3$. In Figs. 5(c) and 5(d), we show the ground-state structure factor at $\nu = 1/3$ and $\nu = 2/3$, respectively, for different values of κ. Similarly to the LL case, at $\nu = 1/3$, the main peak always remains at the $\boldsymbol{\kappa}/\boldsymbol{\kappa}'$ points, but at $\nu = 2/3$, it shifts to a larger momentum when κ is large. This shift is consistent with the dominant CDW instability shifting from a hole to an electron Wigner crystal.

V. ADIABATIC BANDS

By taking both $B_1 \neq 0$ and $U_1 \neq 0$ in Eq. (1), we obtain a pair of dispersive bands with nonideal quantum geometry, as indicated in Fig. 1. The parameter U_1 controls the bandwidth of the $n = 0$ band, which we denote W. As commented above, the many-body physics of the adiabatic model is dictated by three energy scales: $e^2/\varepsilon\ell$, Δ_g, and W. For sufficiently large W, the two lowest bands can invert, changing the Chern number of the $n = 0$ adiabatic band from $C = 1$ to $C = 0$. Since we focus on the FCI ground state, we exclude the topologically trivial regime by restricting to $W \ll \Delta_g$ and tuning the interaction strength via the dielectric constant ε. Moreover, because the interacting state of a fractionally filled $n = 0$ band is expected to be metallic (with a vanishing many-body gap) when $e^2/\varepsilon\ell \lesssim W$, we further confine ourselves to the regime where interactions dominate over the bandwidth.

In Fig. 6, we show the evolution of the many-body gaps at fillings $\nu = 1/3$ and $\nu = 2/3$, for different adiabatic bands. For $\nu = 1/3$, the two-band-projected gaps (lines with dots) are consistently smaller than the one-band-projected gaps (dashed lines). Meanwhile, for $\nu = 2/3$ we can identify a range of κ for which the two-band-projected gap is larger than the one-band-projected gap, which reverses for large enough κ. This behavior follows our observations for Landau levels and AC bands, and can be explained by a level crossing between excited states, as can be seen in Figs. 7(a) and 7(b) for an adiabatic band with $B_1 = 0.25$ and $U_1 = 0.025$. Figures 7(c) and 7(d) show the ground-state structure factors at fillings $\nu = 1/3$ and $\nu = 2/3$ of the same band, which again reveals a shift in the momentum of the main peak of $S(\boldsymbol{q})$ at $\nu = 2/3$. Note also that for all the adiabatic bands considered in Fig. 6, the two-band-projected gaps at $\nu = 2/3$ are larger than those at $\nu = 1/3$, meaning that the FCI at $\nu = 2/3$ is more robust.

VI. CONTINUUM MODEL FOR MOIRÉ TMDS

In this section. we present one-band- and two-band-projected ED results for the continuum model of $tMoTe_2$. Similarly to the case of adiabatic bands, there are three energy scales that determine the many-body physics, namely, the interaction scale $e^2/\varepsilon\ell$ [recall $\ell^2 = (\sqrt{3}/4\pi)a_M^2$], the band gap Δ_g, and the bandwidth of the topmost band W. We have chosen two sets of continuum model parameters. The first model [33] corresponds to parameters $(V, \psi, \omega) = (11.2, -91^\circ, -13.3)$ and twist angle $\theta = 2.0^\circ$. For this model, the two topmost valence bands have the same Chern number, and a recent VMC study [45] found the FCI at $\nu = 2/3$ to be stable to remote band mixing, while the ground state at $\nu = 1/3$ is found to be a CDW. The second model corresponds to parameters $(V, \psi, \omega) = (16.5, -105.9^\circ, -18.8)$ [75] and $\theta = 3.5^\circ$, which is approximately the twist angle of the

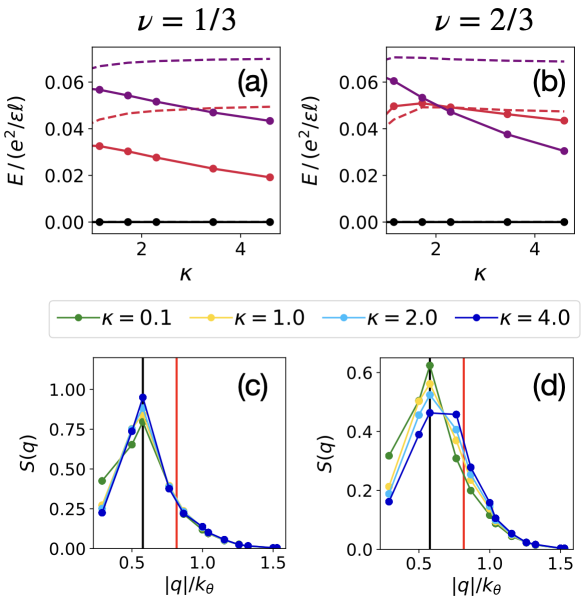


FIG. 7. Evolution of the low-energy many-body states as a function of κ at (a) $\nu = 1/3$ and (b) $\nu = 2/3$ for an adiabatic band with $B_1 = 0.25$ and $U_1 = 0.025$. Dashed lines correspond to single-band-projected calculations and lines with dots to two-band-projected calculations. The color convention is the same as for Fig. 2. Ground-state structure factors at (c) $\nu = 1/3$ and (d) $\nu = 2/3$ for several values of κ. The vertical lines indicate the wave vectors corresponding to the crystal unit cells shown in Fig. 3. The level crossing in panel (b) at filling $\nu = 2/3$ correlates with the shift in the main peak of $S(q)$ in panel (d). Secondary peaks at $|q| = k_\theta$ start developing but are less pronounced than in Fig. 5.

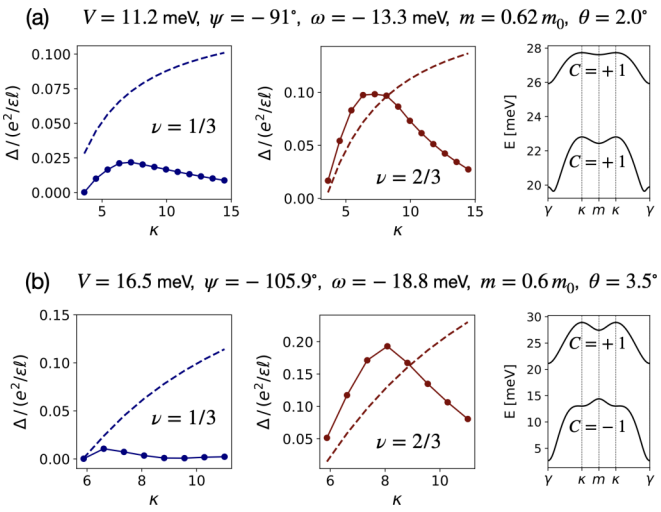


FIG. 8. Exact diagonalization results for two continuum models of $tMoTe_2$. Evolution of the many-body gaps at $\nu = 1/3$ and $\nu = 2/3$ as a function of band mixing. Dashed lines correspond to single-band-projected calculations and lines with dots to two-band-projected calculations. The rightmost panel shows the two topmost K valley noninteracting bands with their respective Chern numbers; the bands emerging from the K' valley are related via time reversal.

sample studied in Ref. [16]. In this model, the Chern numbers of the two topmost moiré bands are opposite.

In Fig. 8, we show the evolution of the many-body gaps at filling fractions $\nu = 1/3$ and $\nu = 2/3$ with respect to band mixing for both continuum models. The behavior of the gaps is qualitatively similar to the ones shown in Fig. 6 for adiabatic bands. The one-band-projected results (dashed lines) are always larger than their two-band-projected counterparts (lines with dots) at $\nu = 1/3$. In contrast, at $\nu = 2/3$ there is a range of κ for which the two-band-projected gap is larger than the one-band-projected gap, which reverses for large enough κ. This behavior can be associated with a level crossing between excited states, as we show in Appendix B. In addition, for a fixed value of κ, the many-body gap at $\nu = 2/3$ is always larger than the gap at $\nu = 1/3$, indicating that the FCI states are more stable at filling fractions $\nu > 1/2$ when band mixing is included, which is consistent with previous ED studies [40,41].

A recent multiband ED study [43] of the model [75] that considers a slightly larger twist angle $\theta = 3.7°$ finds that the magnetoroton gap at $\nu = 2/3$ is nearly unchanged with the inclusion of band mixing. They considered a value of the dielectric constant relevant to experiment, $\varepsilon \approx 11.11$, which translates into $\kappa \sim 9$. This is consistent with our calculation: Figure 8(b) shows that the level crossing between excited energy levels happens very near $\kappa = 9$, and that the one-band- and two-band-projected gaps have similar magnitudes at that point in the phase diagram. This explains the robustness of the FCI at $\nu = 2/3$ seen in Ref. [43]. This is also consistent with the experimental observation of an RIQH effect with $C = 1$ when the density is tuned away from $\nu = 2/3$ [10], since this observation indicates that the main instability is a hole Wigner crystal, which onsets around $\kappa \lesssim 8$ according to our results.

VII. DISCUSSION

Previous work [40–47] has established that incorporating remote bands is essential for correctly reproducing the experimental phenomenology of $tMoTe_2$. However, the mechanism driving this effect was unclear. Motivated by experimental observations of RIQAH states and the particle-hole asymmetry in the phase diagram of $tMoTe_2$, we have investigated the effect of remote band mixing on the nature of the FCI ground states at filling fractions $\nu = 1/3$ and $\nu = 2/3$. By exploiting the mapping between continuum moiré TMD models and an effective Landau level problem [48], we leveraged known results on CDWs in the fractional quantum Hall effect to propose an explanation for the particle-hole asymmetry observed in numerical studies of $tMoTe_2$ continuum Hamiltonians, which may also account for recent experimental findings [16].

All the models that we studied here, namely, Landau levels, AC bands, adiabatic bands, and continuum moiré models, exhibit a larger many-body gap at $\nu = 2/3$ than at $\nu = 1/3$ and a two-step behavior in the multiband projected gap at $\nu = 2/3$ as a function of band mixing. This characteristic behavior of the $\nu = 2/3$ gap is due to a crossing between the two lowest excited energy levels, which we attribute to a change in the dominant CDW instability of the FCI state. In the context of

Landau levels, LL mixing allows for electron Wigner crystals to lower their energy significantly, while the energy of hole Wigner crystals remains largely unchanged [73]. The origin of this asymmetry is that a Wigner crystal can be described as a Slater determinant of localized orbitals centered on a triangular lattice, and enlarging the Hilbert space beyond the lowest Landau level allows these orbitals to become more localized [specifically, the minimal spread decreases from $\sqrt{2}\ell$ in the $n = 0$ level alone to $(4 - 2\sqrt{2})^{1/2}\,\ell$ when the $n = 0$ and $n = 1$ levels are combined], which lowers the electron-crystal energy [76]. A hole crystal cannot benefit in the same way, since holes reside in the filled $n = 0$ level and there is no lower level for them to mix with. Thus, while at filling $\nu = 2/3$ and $\kappa \to 0$, the hole crystal initially has lower energy than the electron crystal [69]; as κ increases, the energy of the electron crystal decreases, and upon reaching a critical value of κ, the electron crystal becomes the lowest-energy competing CDW phase. This transition is reflected in the many-body spectrum by a change in the position of the magnetoroton minimum, and is accompanied by shift in the wave vector where the FQH structure factor is peaked. The increase of the magnetoroton minimum wave vector is consistent with the unit cell of the main competing CDW becoming smaller. A recent VMC study of LLs on the sphere confirms this picture [77]. Going beyond LLs, we have shown that this behavior persists in the AC and adiabatic models and even in some regimes of the continuum model for $tMoTe_2$, although the confluence of finite bandwidth and nontrivial quantum geometry makes it harder to ascribe the particle-hole asymmetry to a single cause. The mechanism described here offers an explanation for why the inclusion of the second band in previous ED studies [40–43] weakens the state at $\nu = 1/3$ more than at $\nu = 2/3$.

It is also worth noting that the impact of band mixing on the FCI ground state may depend on the Chern number and quantum geometry of the remote band. In nearly all cases considered here, the two bands share the same Chern number and can therefore be viewed as deviations from a generalized Landau level structure. However, in certain experimentally relevant twist-angle regimes of $tMoTe_2$, the two topmost bands carry opposite Chern numbers [11,12]—as in the model shown in Fig. 8(b)—for which a Haldane-like description is more appropriate [44]. While such differences in band structure may lead to quantitative modifications, we expect the central mechanism identified here—namely, that remote band mixing preferentially stabilizes electron Wigner crystals over hole Wigner crystals—to remain robust. This provides a natural explanation for the enhanced stability of the $\nu = 2/3$ FCI and the proliferation of RIQAH states in $tMoTe_2$ when the density is slightly away from $\nu = 2/3$.

Here, we assume valley polarization, motivated by recent experimental observations [16]. For completeness, in Appendix B we show an example of ED results including the valley degree of freedom. Studying the behavior of non-valley-polarized states as a function of band mixing [40] is an important direction for future study, but lies beyond the scope of this work. Recently, the composite fermion approach has been adapted to semiconductor moiré materials [78–81]. Incorporating the effect of remote bands into this framework is a natural next step. Finally, we note that disorder and strain effects, which are not included in our study but are present in experiments, may further contribute to the observed particle-hole asymmetry.

ACKNOWLEDGMENTS

We thank Allan H. MacDonald, Zlatko Papić, and Nicolas Regnault for fruitful discussions. This work was performed in part at the Aspen Center for Physics, which was supported by National Science Foundation Grant No. PHY-2210452. J.S. acknowledges support by the US Department of Energy, Office of Science, Basic Energy Sciences, Materials Sciences and Engineering Division. C.V. acknowledges support by the Leverhulme Trust Research Leadership Award No. RL-2019-015 and EPSRC Grants No. EP/Z533634/1 and No. UKRI1337. P.P. acknowledges the Texas Advanced Computing Center (TACC) at The University of Texas at Austin for providing high-performance computer resources. J.C. acknowledges support from the Air Force Office of Scientific Research under Grant No. FA9550-24-1-0222. The Flatiron Institute is a division of the Simons Foundation.

Statement of compliance with EPSRC policy framework on research data: This publication is theoretical work that does not require supporting research data.

DATA AVAILABILITY

The data that support the findings of this article are not publicly available. The data are available from the authors upon reasonable request.

APPENDIX A: CONNECTION BETWEEN THE ADIABATIC MODEL AND THE CONTINUUM MODEL FOR SEMICONDUCTOR MOIRÉ MATERIALS

Here, we briefly explain how the continuum model for $tMoTe_2$ [82] and the different models studied in this work are related. Full details are provided in Refs. [48,49]. The K-valley-projected continuum model for TMD homobilayers is written in layer space as

$$H^K_{\mathrm{TMD}} = \begin{pmatrix} -\frac{\hbar^2}{2m^*}(\boldsymbol{k}-\boldsymbol{k}_b)^2 + \Delta_b(\boldsymbol{r}) & \Delta_T(\boldsymbol{r}) \\ \Delta_T^\dagger(\boldsymbol{r}) & -\frac{\hbar^2}{2m^*}(\boldsymbol{k}-\boldsymbol{k}_t)^2 + \Delta_t(\boldsymbol{r}) \end{pmatrix}. \tag{A1}$$

We can apply a gauge transformation $S = \mathrm{diag}(e^{i\boldsymbol{k}_b\cdot\boldsymbol{r}}, e^{i\boldsymbol{k}_t\cdot\boldsymbol{r}})$ to remove the momentum shifts on the diagonal, so that the continuum Hamiltonian can be expressed in terms of layer Pauli matrices as

$$S^\dagger H^K_{\mathrm{TMD}} S = -\frac{1}{2m}\boldsymbol{k}^2\sigma_0 + \boldsymbol{\Delta}(\boldsymbol{r})\cdot\boldsymbol{\sigma} + \Delta_0\sigma_0, \tag{A2}$$

where σ_0 is the identity, $\boldsymbol{\sigma} = (\sigma_x, \sigma_y, \sigma_z)$ is the vector of Pauli matrices, and

$$\boldsymbol{\Delta} = (\mathrm{Re}\Delta_T, \mathrm{Im}\Delta_T, [\Delta_t - \Delta_b]/2), \quad \Delta_0 = [\Delta_t + \Delta_b]/2. \tag{A3}$$

TABLE I. Details about the finite-size torus geometries used in this work. The Brillouin zone discretizations are shown in the insets of Fig. 9, with the corresponding label indicated.

Label	$(\alpha_{11}, \alpha_{12}, \alpha_{21}, \alpha_{22})$	$(N_1^{\rm rec}, N_2^{\rm rec})$	$\tilde{\boldsymbol{v}}_1$	$\tilde{\boldsymbol{v}}_2$
12A	$(2, -2, 3, 3)$	$(6, 2)$	$\boldsymbol{b}_1/6 - \boldsymbol{b}_2/3$	$\boldsymbol{b}_2/2$
12B	$(3, 0, 0, 4)$	$(3, 4)$	$\boldsymbol{b}_1/3$	$\boldsymbol{b}_2/4$
12C	$(2, -2, 4, 2)$	$(4, 3)$	$\boldsymbol{b}_1/4 - \boldsymbol{b}_2/4$	$-\boldsymbol{b}_1/3 + 2\boldsymbol{b}_1/3$
15A	$(3, 0, 0, 5)$	$(3, 5)$	$\boldsymbol{b}_1/3$	$\boldsymbol{b}_2/5$

We apply a unitary transformation to the Hamiltonian [Eq. (A2)] such that at every position the vector field $\boldsymbol{\Delta}(\boldsymbol{r})$ is rotated to point to the $+z$ direction, namely,

$$U^\dagger(\boldsymbol{r})\boldsymbol{\Delta}(\boldsymbol{r})U(\boldsymbol{r}) = |\boldsymbol{\Delta}(\boldsymbol{r})|\sigma_z, \tag{A4}$$

after which the transformed Hamiltonian reads

$$\begin{aligned} U^\dagger S^\dagger \left(H^K_{\rm TMD}\right) SU \equiv \tilde{H}^K_{\rm TMD} \\ = -\frac{1}{2m^*}\begin{pmatrix} \hbar\boldsymbol{k} + e\tilde{\boldsymbol{A}}_{++} & e\tilde{\boldsymbol{A}}_{+-} \\ e\tilde{\boldsymbol{A}}_{-+} & \hbar\boldsymbol{k} + e\tilde{\boldsymbol{A}}_{--} \end{pmatrix}^2 \\ + \begin{pmatrix} \tilde{\Delta}_+ & 0 \\ 0 & \tilde{\Delta}_- \end{pmatrix}. \end{aligned} \tag{A5}$$

Here, $\tilde{\boldsymbol{A}} = -U^\dagger \nabla U$ is a non-Abelian vector potential and $\tilde{\Delta}_\pm = \pm|\boldsymbol{\Delta}| + \Delta_0$. The adiabatic approximation consists of truncating the 2×2 Hamiltonian in Eq. (A5) to just the high-energy block. It describes dilute filling of the first moiré valence band in the limit $|\boldsymbol{\Delta}| \gg \hbar^2/2m^* a_M^2$.

The truncation to the "++" block yields the Hamiltonian of a particle in the presence of a periodic magnetic field and a periodic potential

$$H^K_{\rm adiabatic} = -\frac{1}{2m^*}[\hbar\boldsymbol{k} + e\tilde{\boldsymbol{A}}_{++}(\boldsymbol{r})]^2 - D(\boldsymbol{r}) + \tilde{\Delta}_+(\boldsymbol{r}), \tag{A6}$$

where $D(\boldsymbol{r}) = (e^2/2m^*)\tilde{\boldsymbol{A}}_{+-} \cdot \tilde{\boldsymbol{A}}_{-+}$ is known as the *kinetic potential* [48]. The Hamiltonian above can be reorganized as

$$H^K_{\rm adiabatic} = -\frac{1}{2m^*}\Pi_-\Pi_+ + \tilde{\Delta}(\boldsymbol{r}) - D(\boldsymbol{r}) + \frac{B(\boldsymbol{r})}{2m^*}, \tag{A7}$$

with the kinetic-momentum operators $\Pi_\pm$ as defined in the main text. Equation (A7) is precisely the *adiabatic Hamiltonian* that we study in our article, i.e., Eq. (1), with

$$U(\boldsymbol{r}) \equiv \tilde{\Delta}(\boldsymbol{r}) - D(\boldsymbol{r}) + \frac{B(\boldsymbol{r})}{2m^*}. \tag{A8}$$

APPENDIX B: ADDITIONAL EXACT DIAGONALIZATION RESULTS

In this Appendix, we present additional ED results on different geometries and system sizes to complement the results reported in the main text.

1. Torus geometry

We consider a finite system (supercell) consisting of N unit cells of the periodic functions $B(\boldsymbol{r})$ and $U(\boldsymbol{r})$ and apply periodic boundary conditions. The supercell is generated by the vectors $\boldsymbol{T}_i$, which are linear combinations of the primitive lattice vectors $\boldsymbol{R}_i$,

$$\begin{pmatrix} \boldsymbol{T}_1 \\ \boldsymbol{T}_2 \end{pmatrix} = \begin{pmatrix} \alpha_{11} & \alpha_{12} \\ \alpha_{21} & \alpha_{22} \end{pmatrix}\begin{pmatrix} \boldsymbol{R}_1 \\ \boldsymbol{R}_2 \end{pmatrix}. \tag{B1}$$

A given supercell corresponds to a particular discretization of the Brillouin zone that we use for momentum space ED. The discretization is obtained by first defining the vectors $\boldsymbol{v}_i$ via $\boldsymbol{v}_i \cdot \boldsymbol{T}_j = 2\pi\,\delta_{ij}$, and then the integers

$$N_1^{\rm rec} = \frac{N}{\mathrm{GCD}(N, \alpha_{22}, \alpha_{21})} \quad \text{and} \quad N_2^{\rm rec} = \mathrm{GCD}(N, \alpha_{22}, \alpha_{21}). \tag{B2}$$

The generating vectors of the Brillouin zone discretization are

$$\tilde{\boldsymbol{v}}_1 = \boldsymbol{v}_1 \quad \text{and} \quad \tilde{\boldsymbol{v}}_2 = \boldsymbol{v}_2 + \alpha_{\rm rec}\boldsymbol{v}_1, \tag{B3}$$

where $\alpha_{\rm rec}$ is the solution to the equations [83,84]

$$\begin{aligned} \alpha_{11} - \alpha_{\rm rec}\,\alpha_{21} &= N_1^{\rm rec}\, l_1, \\ \alpha_{12} - \alpha_{\rm rec}\,\alpha_{22} &= N_1^{\rm rec}\, l_2, \end{aligned}$$

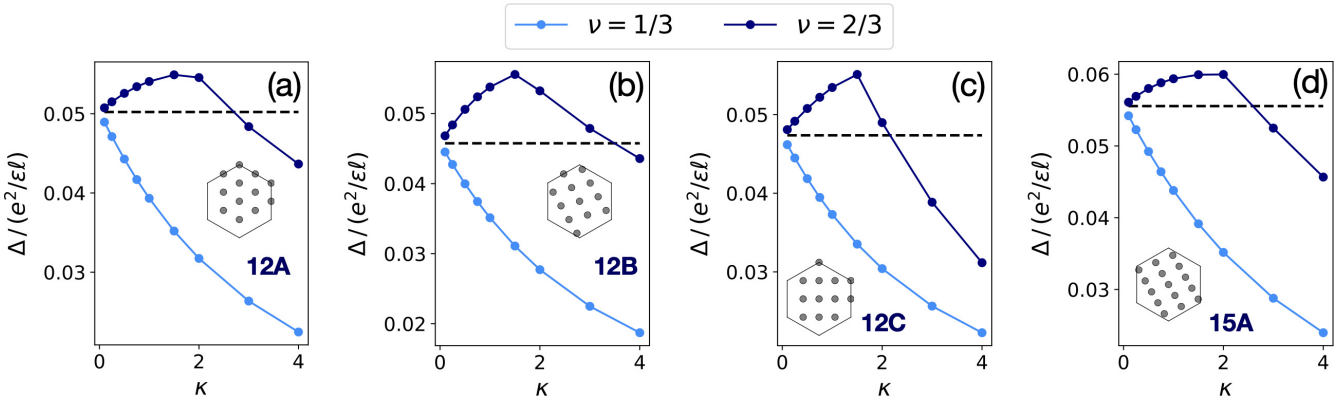


FIG. 9. Exact diagonalization results on Landau levels for different Brillouin zone discretizations. One-band-projected (dashed line) and two-band-projected (lines with dots) many-body gaps for fillings $\nu = 1/3, 2/3$ as a function of LL mixing. The insets indicate the geometry used for calculations. Panel (a)–(c) correspond to $N = 12$ unit cells and panel (d) to $N = 15$ unit cells, as described in Table I. We recover the same contrasting behavior between $\nu = 2/3$ and $\nu = 1/3$ in all the system sizes and discretizations that we study.

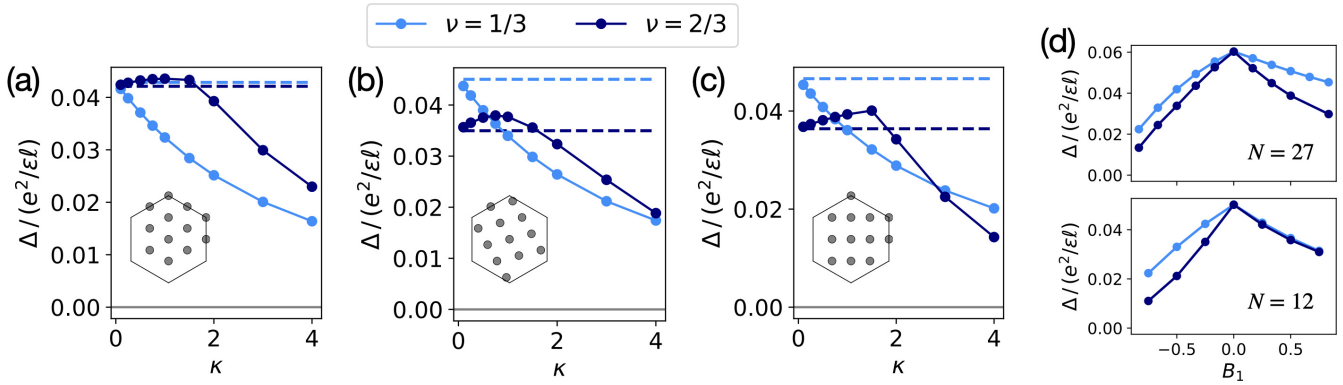


FIG. 10. Particle-hole asymmetry above and below $\nu = 1/2$ in an AC band with $B_1 = 0.25$. (a)–(c) Evolution of the many-body gap at fillings $\nu = 1/3$ and $\nu = 2/3$, as a function of κ and for different Brillouin zone discretizations that are indicated in the insets. (d) Evolution of the one-band-projected many-body gaps as a function of B_1 for two system sizes. The asymmetry with respect to the sign of B_1 becomes less pronounced as system size increases. For all the AC models studied here, the gap at $\nu = 1/3$ is greater than its counterpart at $\nu = 2/3$ at the single-band-projected level.

where l_1, l_2 are integers. The accessible momenta in the Brillouin zone are given by

$$\begin{aligned} \boldsymbol{k} &= \frac{n_1}{N_1^{\mathrm{rec}}}\,\tilde{\boldsymbol{v}}_1 + \frac{n_2}{N_2^{\mathrm{rec}}}\,\tilde{\boldsymbol{v}}_2, \\ n_1 &= 0, \ldots, N_1^{\mathrm{rec}} - 1, \\ n_2 &= 0, \ldots, N_2^{\mathrm{rec}} - 1. \end{aligned} \tag{B4}$$

Table I indicates the different finite-size geometries with periodic boundary conditions used for our calculations. We choose the reciprocal lattice vectors to be $\boldsymbol{b}_1 = k_\theta(1/2, \sqrt{3}/2)$ and $\boldsymbol{b}_1 = k_\theta(-1/2, \sqrt{3}/2)$, $k_\theta = 4\pi/\sqrt{3}a_M$.

In Fig. 9, we show the evolution of the many-body gap at fillings $\nu = 1/3$ and $\nu = 2/3$ of Landau levels, as a function of κ. We present results for different choices of periodic boundary conditions, which translate into different discretizations of the Brillouin zone. We observe that the behavior of the gaps at $\nu = 1/3$ and $\nu = 2/3$ is consistent across all systems studied.

In Fig. 10, we show the evolution of the many-body gap as a function of κ for an AC band with $B_1 = 0.25$ and for different Brillouin zone discretizations in a system with $N = 12$ unit cells. As commented in the main text, because the Berry curvature is not uniform, the particle-hole symmetry is already broken at the single-band-projected level, which is manifested in the two dashed lines not coinciding. We see that the amount of particle-hole asymmetry at the single-band-projected level depends on the Brillouin zone discretization. Despite this, the effect of remote bands on particle-hole asymmetry is always consistent.

In Fig. 11, we show the many-body spectra obtained in the limit $\hbar\omega_c \to 0$ when the $n = 0$ and $n = 1$ Landau levels are exactly degenerate, for both filling fractions $\nu = 1/3$ and $\nu = 2/3$. This limit applies to the zeroth LL of bilayer graphene and we use it as a sanity check for our numerics. In agreement with previous experimental and numerical studies [63–67], we recover that the gap at $\nu = 2/3$ is larger than its counterpart at $\nu = 1/3$. In Fig. 11, we also show the many-body spectra for the largest value of κ considered in the main text ($\kappa = 4$). We see that the many-body spectrum evolves adiabatically from $\kappa = 4$ up to $\kappa \to \infty$ at both filling fractions.

In Fig. 12, we show the evolution of momentum occupations as a function of κ for Landau levels. We define the momentum occupations in each band as $n_m = \frac{1}{N}\sum_{\boldsymbol{k}} n_m(\boldsymbol{k})$, where $m = 0, 1$ is the band index. We include the ground state occupations and also the occupations corresponding to the excitations at the $\boldsymbol{\gamma}, \boldsymbol{\kappa}, \boldsymbol{\kappa}'$ points ("Roton 1," indicated in red in Fig. 2) and the occupations corresponding to the excitations at the other nine momentum points ("Roton 2," indicated in purple in Fig. 2). We see that the ground state and the low-energy excitations almost completely occupy the lowest band for both fillings.

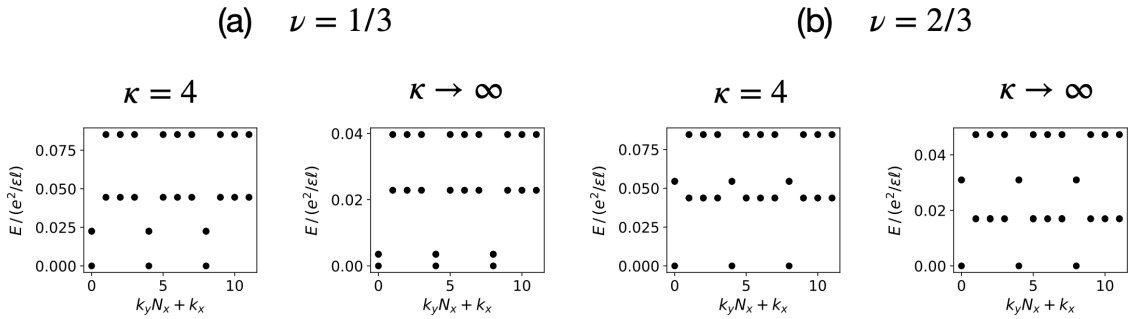


FIG. 11. Comparison between many-body spectra with band-mixing parameters $\kappa = 4$ and $\hbar\omega_c = 0$ (that we label as $\kappa \to \infty$) for (a) $\nu = 1/3$ and (b) $\nu = 2/3$ for the case of Landau levels, namely, $B_1 = U_1 = 0$ in Eq. (1).

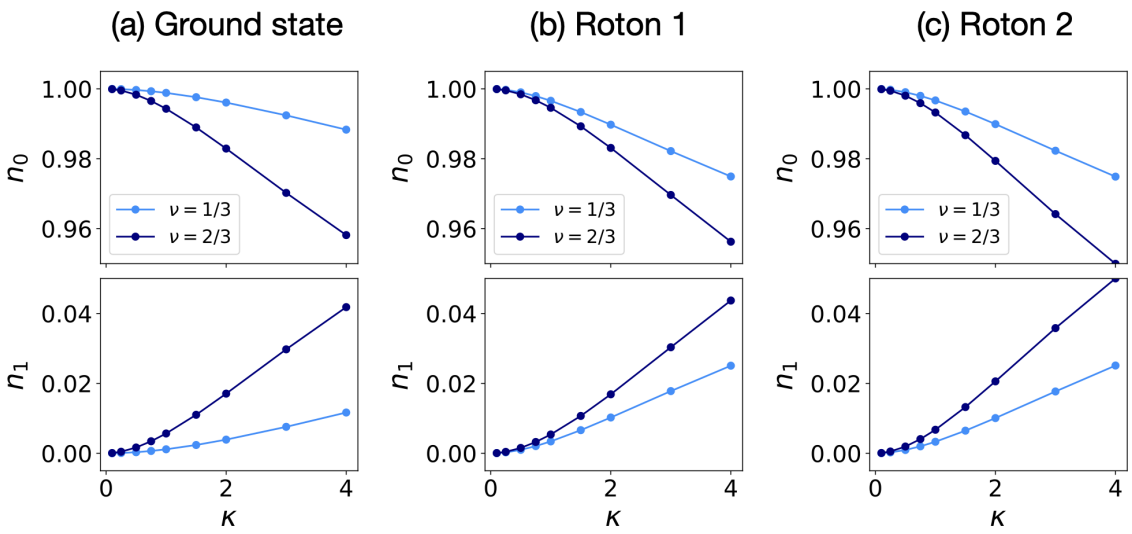


FIG. 12. Momentum occupation of many-body states as a function of κ and at fillings $\nu = 1/3$ and $\nu = 2/3$ of a two-band system with $B_1 = U_1 = 0$. Panels (a)–(c) correspond to the states indicated in black, red, and purple in Fig. 1, respectively.

We also analyze the effects of screening on our results. In Fig. 13, we show the evolution of the many-body gaps at fillings $\nu = 1/3$ and $\nu = 2/3$ for screened Coulomb interactions corresponding to metallic gates at distances $d = 10$ nm, $d = 15$ nm, and $d = 20$ nm. We see that the many-body gaps for the LLL and AC bands display the same qualitative behavior as for the unscreened case presented in the main text. The magnitude of the many-body gaps decreases as the gates are made closer, which is in agreement with results for continuum models of $tMoTe_2$ presented in Ref. [35]. In Fig. 14, we show the evolution of the many-body gaps at fillings $\nu = 1/3$ and $\nu = 2/3$ when the interaction term is given by the first Haldane pseudopotential. The results are in qualitative agreement with those in the main text obtained using the Coulomb interaction. For the case of Landau levels, Fig. 14(a), the one-band-projected gaps (dashed lines) coincide, as expected. The two-band-projected gap at $\nu = 1/3$ decreases monotonically, and the two-band-projected gap at $\nu = 2/3$ shows a first increasing and then decreasing behavior, although the level crossing happens at a very small value of κ. This can be explained by the fact that the magnetoroton dispersion is almost flat for the Haldane pseudopotential interaction [68], as can be seen in the many-body spectra shown in Fig. 14(c). Results for an AC band with $B_1 = 0.25$ are shown in Fig. 14(b). The particle-hole symmetry is broken at the single-band-projected level due to the nonuniform quantum geometry of the band. We again observe the nonmonotonic behavior of the two-band-projected gap at $\nu = 2/3$. A recent single-band ED study on AC bands [85] finds a superconducting ground state at $\nu = 2/3$ for large enough values of B_1. The effect of remote bands on the stability of that superconducting state is an interesting direction for future research.

Motivated by the experimental observation of valley polarization across a range of fillings of the topmost band of $tMoTe_2$, we have assumed valley polarization for our study. For completeness, in Fig. 15 we show ED calculations including the other valley degree of freedom. We continue to observe the same trend described in our single-valley calculations: The

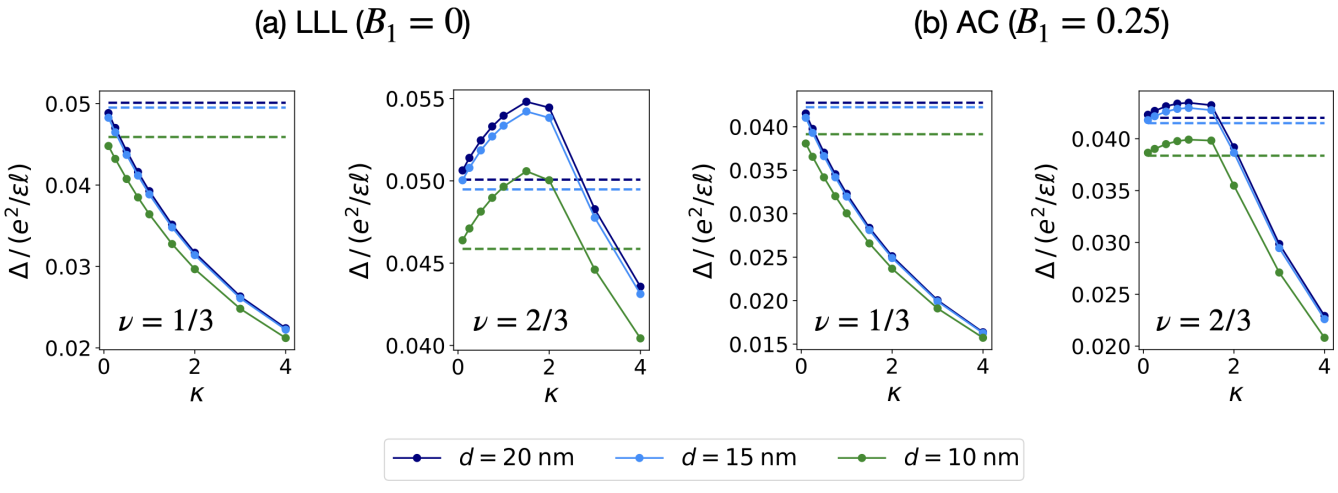


FIG. 13. Effects of a screened Coulomb interaction, $V(\boldsymbol{q}) = 2\pi e^2 \tanh(qd)/\varepsilon\boldsymbol{q}$. Evolution of the many-body gap as a function of band mixing for (a) the LLL at fillings $\nu = 1/3$ and $\nu = 2/3$ and (b) an AC band at fillings $\nu = 1/3$ and $\nu = 2/3$.

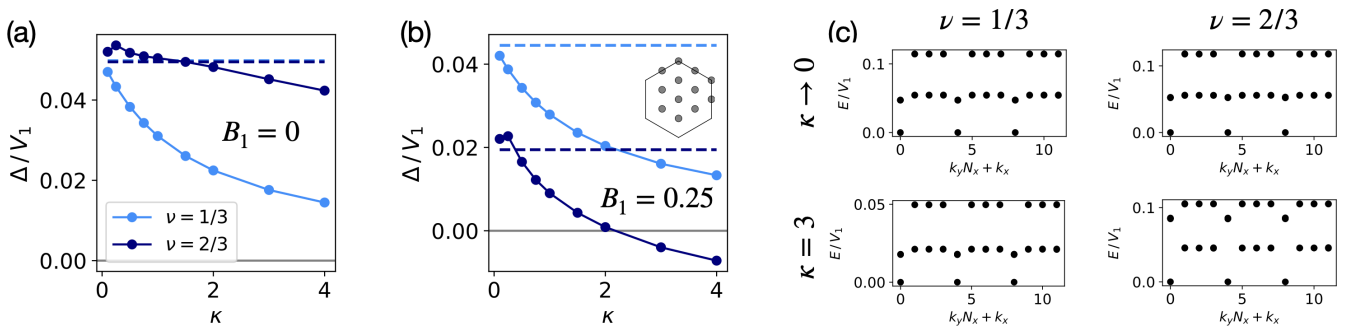


FIG. 14. Evolution of the many-body gaps as a function of band mixing for (a) Landau levels and (b) an AC band with $B_1 = 0.25$, using the Haldane pseudopotential interaction $V(\boldsymbol{q}) = -V_1\boldsymbol{q}^2$. Dashed lines are one-band-projected calculations and lines with dots are two-band-projected calculations. (c) Typical many-body spectra for Landau levels at filling fractions $\nu = 1/3$ and $\nu = 2/3$ for two values of κ.

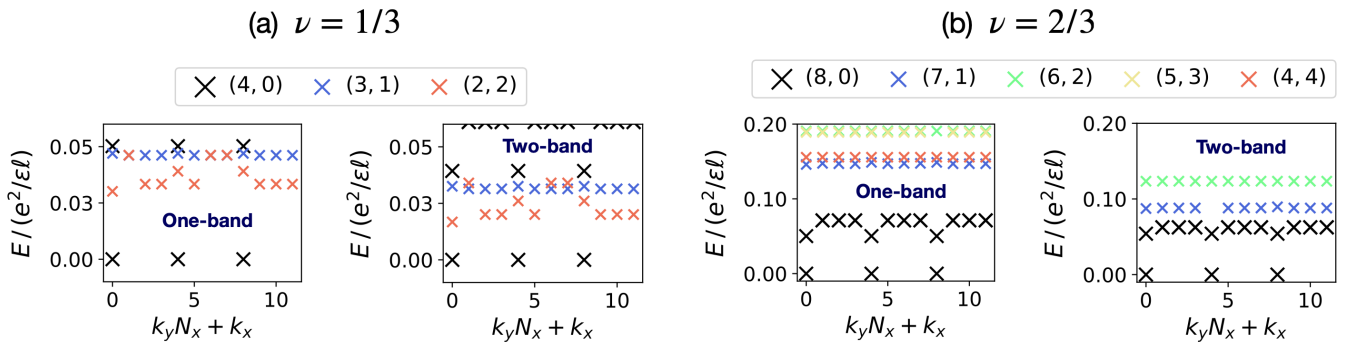


FIG. 15. Exact diagonalization calculations at (a) $\nu = 1/3$ and (b) $\nu = 2/3$ for a system with $B_1 = 0$, $U_1 = 0$, and $\kappa = 1.0$, including one and two bands per valley. Each sector $(N_K, N_{K'})$, corresponding to N_K particles in valley K and $N_{K'}$ particles in valley K', is indicated in a different color. For the two-band-per-valley calculation at $\nu = 2/3$, the sectors (5, 3) and (4, 4) are beyond the scope of our computational resources and hence are not included.

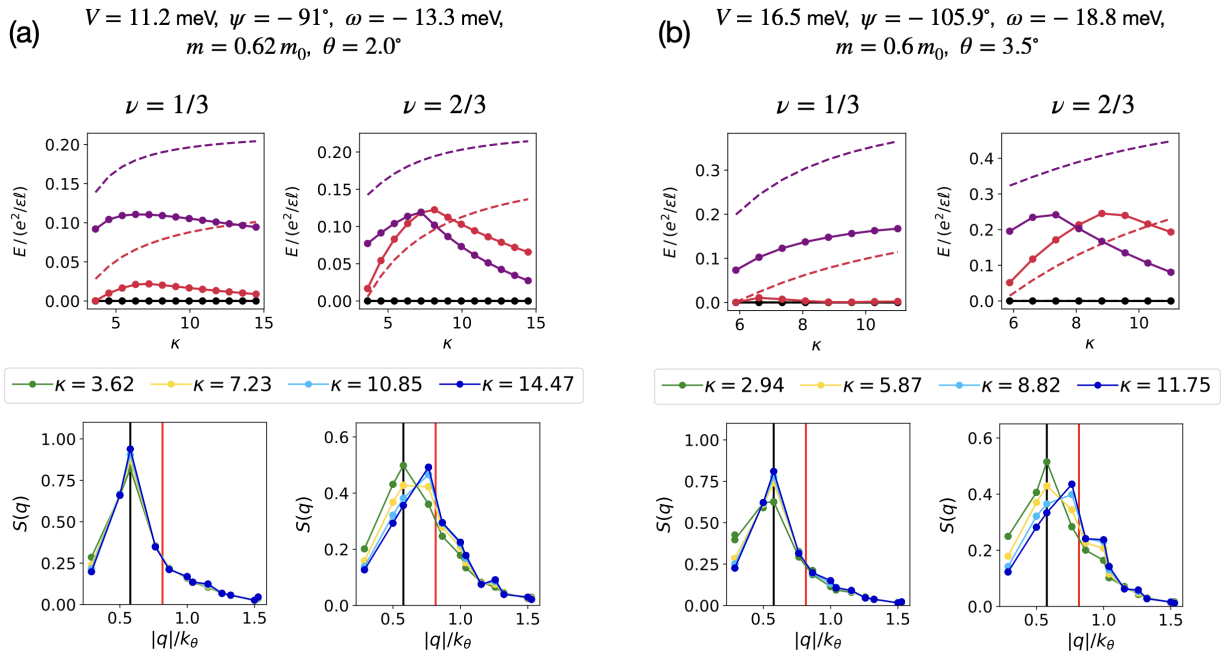


FIG. 16. Top panel: Evolution of the low-energy many-body states as a function of κ at $\nu = 1/3$ and $\nu = 2/3$ for the two continuum models of $tMoTe_2$ studied here. Dashed lines correspond to single-band-projected calculations and lines with dots to two-band-projected calculations. The color convention is the same as in the main text. A level crossing can be observed at $\nu = 2/3$ in both models. Bottom panel: Ground-state structure factors for several values of κ, exhibiting a change in the position of the main peak at $\nu = 2/3$ for both continuum models.

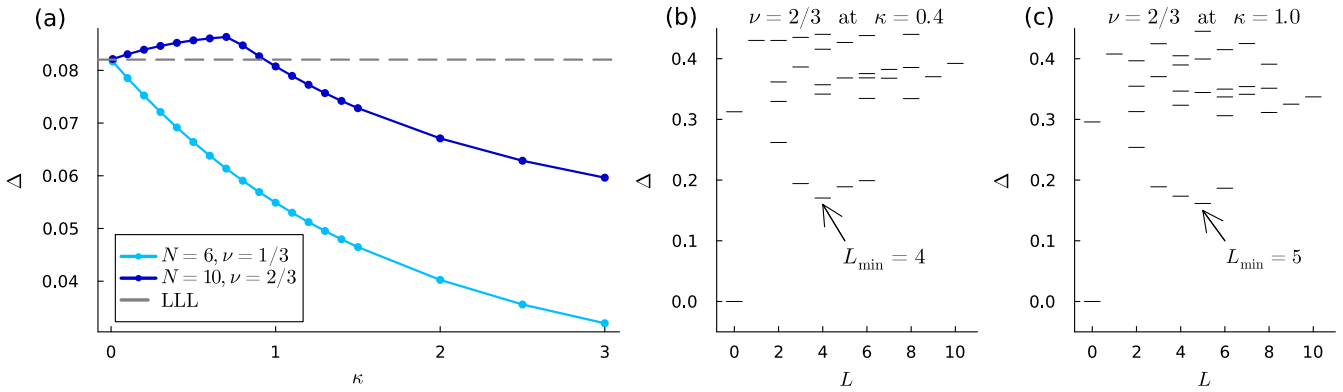


FIG. 17. Exact diagonalization results on the sphere. The two conjugate filling factors are studied for the same number of flux quanta, $2Q = 15$. (a) Many-body gap as a function of the band-mixing parameter κ. Similarly to the torus geometry, at $\nu = 1/3$, the gap decays monotonically, while at $\nu = 2/3$, the gap increases until $\kappa \approx 0.7$ and then decreases. (b), (c) The low-energy spectrum at $\nu = 2/3$ for values of κ above and below the critical value $\kappa \approx 0.7$, resolved by total angular momentum L. The change in the behavior of the many-body gap near $\kappa \approx 0.7$ corresponds to a change in the location of the magnetoroton minimum from $L = 4$ ($\kappa < 0.7$) to $L = 5$ ($\kappa > 0.7$).

many-body gap at $\nu = 1/3$ decreases monotonically with κ, while the many-body gap at $\nu = 2/3$ first increases and then decreases as a function of κ.

Finally, in Fig. 16 we show the evolution of the low-lying many-body energies and the structure factors as a function of the mixing parameter κ for the two continuum models of $tMoTe_2$ studied in the main text. The behavior is in qualitative agreement with the LL, AC, and adiabatic models. For two-band-projected calculations, the lowest excited state always remains in the same momentum sector at $\nu = 1/3$, while there is a level crossing between the two lowest excited states, which belong to different momentum sectors, at $\nu = 2/3$. The structure factor peaks at $\nu = 2/3$ shift to a larger wave vector for large κ, as also observed for LL, AC, and adiabatic models.

2. Spherical geometry

In this Appendix, we show results obtained in the spherical geometry. In this setup, a magnetic monopole is placed at the center of the sphere [86], such that the number of magnetic flux quanta is $2Q = \nu^{-1}N - S$ and the number of available orbitals is $N_\phi = 2Q + 1$. Here, S stands for the Wen-Zee shift [87], which for states in the Jain sequence at $\nu = n/(2pn \pm 1)$ takes the value $S = 2p \pm n$. The single-particle Hamiltonian is that of Eq. (1), restricted to the case of Landau levels by taking $B_1 = U_1 = 0$.

The effect of band mixing on the many-body gap at filling fractions $\nu = 1/3$ and $\nu = 2/3$ is displayed in Fig. 17, showing remarkable agreement with the behavior of the many-body

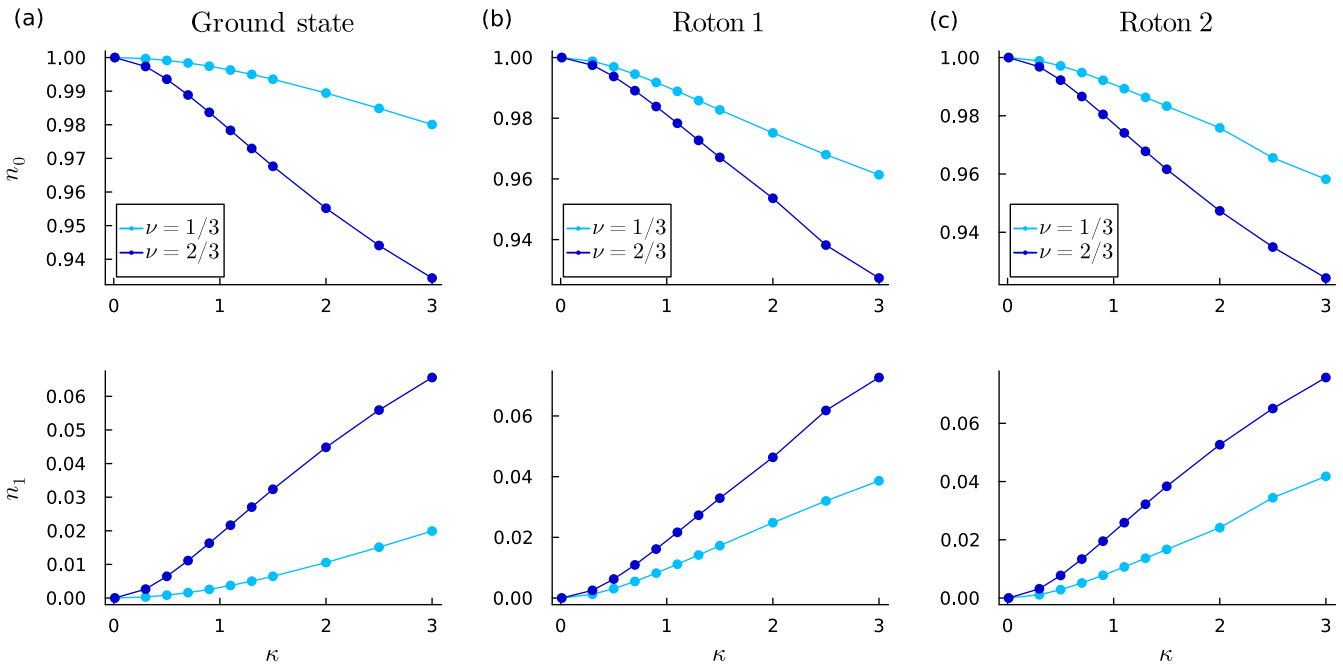


FIG. 18. Band occupations of the ground state and competing roton states [panels (a)–(c), respectively] as a function of the band mixing parameter κ at fillings $\nu = 1/3$ and $\nu = 2/3$. Similar to the torus geometry, occupation of the LLL remains dominant for a significant interval of κ even after the level crossing.

gap on the torus shown in Fig. 2. Specifically, the kink in the many-body gap around $\kappa \approx 0.7$ [Fig. 17(a)] corresponds to a shift in the magnetoroton minimum from $L_{\min} = 4$ to $L_{\min} = 5$ [Figs. 17(b) and 17(c)]. The increase in angular momentum of the minimum is consistent with the electron crystal, which has a smaller unit cell at $\nu = 2/3$, becoming favorable at larger values of the band-mixing parameter κ. For the values of κ considered, the occupation of the LLL remains dominant, as can be seen in Fig. 18, justifying the use of a two-band model approximation.

The change in the location of the magnetoroton minimum on the sphere can be understood as follows. Competing crystalline states are dictated by Thomson configurations [88,89]—in the thermodynamic limit they approach the triangular lattice, while in small systems there can be several competitive configurations, usually possessing large rotational symmetry. Numerically, these symmetry-broken states manifest through a "tower of states," with low-lying states present in the angular momentum sectors allowed by the remaining symmetry subgroup of SO(3). Let us now specialize to $2Q = 15$, corresponding to the calculations in Fig. 17. The electron crystal at $\nu = 1/3$ and hole crystal at $\nu = 2/3$ both form octahedra ($N = 6$ vertices) that are very stable due to the large rotation symmetry group. The first allowed multipole moments in the corresponding tower of states are $L = 4, 6, 8, \ldots$, which is why the minimum occurs at $L = 4$ for $\kappa \lesssim 0.7$ in Fig. 17. After the level crossing at $\nu = 2/3$, the roton minimum moves to $L = 5$, which is forbidden for the hole crystal but allowed for the electron crystal, i.e., the $N = 10$ Thomson configurations.

[1] J. Cai, E. Anderson, C. Wang, X. Zhang, X. Liu, W. Holtzmann, Y. Zhang, F. Fan, T. Taniguchi, K. Watanabe, Y. Ran, T. Cao, L. Fu, D. Xiao, W. Yao, and X. Xu, Signatures of fractional quantum anomalous Hall states in twisted $MoTe_2$, Nature (London) **622**, 63 (2023).

[2] Y. Zeng, Z. Xia, K. Kang, J. Zhu, P. Knüppel, C. Vaswani, K. Watanabe, T. Taniguchi, K. F. Mak, and J. Shan, Thermodynamic evidence of fractional Chern insulator in moiré $MoTe_2$, Nature (London) **622**, 69 (2023).

[3] H. Park, J. Cai, E. Anderson, Y. Zhang, J. Zhu, X. Liu, C. Wang, W. Holtzmann, C. Hu, Z. Liu, T. Taniguchi, K. Watanabe, J.-H. Chu, T. Cao, L. Fu, W. Yao, C.-Z. Chang, D. Cobden, D. Xiao, and X. Xu, Observation of fractionally quantized anomalous Hall effect, Nature (London) **622**, 74 (2023).

[4] F. Xu, Z. Sun, T. Jia, C. Liu, C. Xu, C. Li, Y. Gu, K. Watanabe, T. Taniguchi, B. Tong, J. Jia, Z. Shi, S. Jiang, Y. Zhang, X. Liu, and T. Li, Observation of integer and fractional quantum anomalous Hall effects in twisted bilayer $MoTe_2$, Phys. Rev. X **13**, 031037 (2023).

[5] K. Kang, B. Shen, Y. Qiu, Y. Zeng, Z. Xia, K. Watanabe, T. Taniguchi, J. Shan, and K. F. Mak, Evidence of the fractional quantum spin Hall effect in moiré $MoTe_2$, Nature (London) **628**, 522 (2024).

[6] E. Redekop, C. Zhang, H. Park, J. Cai, E. Anderson, O. Sheekey, T. Arp, G. Babikyan, S. Salters, K. Watanabe, T. Taniguchi, M. E. Huber, X. Xu, and A. F. Young, Direct magnetic imaging of fractional Chern insulators in twisted $MoTe_2$, Nature (London) **635**, 584 (2024).

[7] Z. Ji, H. Park, M. E. Barber, C. Hu, K. Watanabe, T. Taniguchi, J.-H. Chu, X. Xu, and Z.-X. Shen, Local probe of bulk and edge states in a fractional Chern insulator, Nature (London) **635**, 578 (2024).

[8] E. Anderson, J. Cai, A. P. Reddy, H. Park, W. Holtzmann, K. Davis, T. Taniguchi, K. Watanabe, T. Smolenski, A. Imamoğlu, T. Cao, D. Xiao, L. Fu, W. Yao, and X. Xu, Trion sensing of a zero-field composite Fermi liquid, Nature (London) **635**, 590 (2024).

[9] Y. Wang, J. Choe, E. Anderson, W. Li, J. Ingham, E. A. Arsenault, Y. Li, X. Hu, T. Taniguchi, K. Watanabe, X. Roy, D. Basov, D. Xiao, R. Queiroz, J. C. Hone, X. Xu, and X.-Y. Zhu, Hidden states and dynamics of fractional fillings in twisted $MoTe_2$ bilayers, Nature (London) **641**, 1149 (2025).

[10] F. Xu, Z. Sun, J. Li, C. Zheng, C. Xu, J. Gao, T. Jia, K. Watanabe, T. Taniguchi, B. Tong, L. Lu, J. Jia, Z. Shi, S. Jiang, Y. Zhang, Y. Zhang, S. Lei, X. Liu, and T. Li, Signatures of unconventional superconductivity near reentrant and fractional quantum anomalous Hall insulators, arXiv:2504.06972.

[11] H. Park, J. Cai, E. Anderson, X.-W. Zhang, X. Liu, W. Holtzmann, W. Li, C. Wang, C. Hu, Y. Zhao, *et al.*, Ferromagnetism and topology of the higher flat band in a fractional Chern insulator, Nat. Phys. **21**, 549 (2025).

[12] F. Xu, X. Chang, J. Xiao, Y. Zhang, F. Liu, Z. Sun, N. Mao, N. Peshcherenko, J. Li, K. Watanabe, T. Taniguchi, B. Tong, L. Lu, J. Jia, D. Qian, Z. Shi, Y. Zhang, X. Liu, S. Jiang, and T. Li, Interplay between topology and correlations in the second moiré band of twisted bilayer $MoTe_2$, Nat. Phys. **21**, 542 (2025).

[13] E. Thompson, K. T. Chu, F. Mesple, X.-W. Zhang, C. Hu, Y. Zhao, H. Park, J. Cai, E. Anderson, K. Watanabe, T. Taniguchi, J. Yang, J.-H. Chu, X. Xu, T. Cao, D. Xiao, and M. Yankowitz, Microscopic signatures of topology in twisted $MoTe_2$, Nat. Phys. **21**, 1224 (2025).

[14] Y. Deng, W. Holtzmann, Z. Zhu, T. Zaklama, P. Majchrzak, T. Taniguchi, K. Watanabe, M. Hashimoto, D. Lu, C. Jozwiak, A. Bostwick, E. Rotenberg, L. Fu, T. P. Devereaux, X. Xu, and Z.-X. Shen, Nonmonotonic band flattening near the magic angle of twisted bilayer $MoTe_2$, Phys. Rev. X **15**, 041043 (2025).

[15] W. Li, E. Redekop, C. Wang Beach, C. Zhang, X. Zhang, X. Liu, W. Holtzmann, C. Hu, E. Anderson, H. Park, T. Taniguchi, K. Watanabe, J.-H. Chu, L. Fu, T. Cao, D. Xiao, A. F. Young, and X. Xu, Universal magnetic phases in twisted bilayer $MoTe_2$, Nano Lett. **25**, 18044 (2025).

[16] H. Pan, S. Yang, Y. Wang, X. Cai, W. Wang, Y. Zhao, K. Watanabe, T. Taniguchi, L. Zhang, Y. Liu, B. Yang, and W. Gao, Optical signatures of $-\frac{1}{3}$ fractional quantum anomalous Hall state in twisted $MoTe_2$, Phys. Rev. Lett. **136**, 056601 (2026).

[17] O. Huber, K. Kuhlbrodt, E. Anderson, W. Li, K. Watanabe, T. Taniguchi, M. Kroner, X. Xu, A. Imamoğlu, and T. Smoleński, Optical control over topological Chern number in moiré materials, Nature (London) **649**, 1153 (2026).

[18] H. Park, W. Li, C. Hu, C. Beach, M. Gonçalves, J. F. Mendez-Valderrama, J. Herzog-Arbeitman, T. Taniguchi, K. Watanabe, D. Cobden, L. Fu, B. A. Bernevig, N. Regnault, J.-H. Chu,

D. Xiao, and X. Xu, Observation of dissipationless fractional Chern insulator, Nat. Phys. **22**, 389 (2026).

[19] W. Holtzmann, W. Li, E. Anderson, J. Cai, H. Park, C. Hu, T. Taniguchi, K. Watanabe, J.-H. Chu, D. Xiao, T. Cao, and X. Xu, Optical control of integer and fractional Chern insulators, Nature (London) **649**, 1147 (2026).

[20] W. Li, C. Wang Beach, C. Hu, T. Taniguchi, K. Watanabe, J.-H. Chu, A. Imamoğlu, T. Cao, D. Xiao, and X. Xu, Signatures of fractional charges via anyon–trions in twisted $MoTe_2$, Nature (London) **651**, 48 (2026).

[21] C. Chen, W. Holtzmann, X.-W. Zhang, E. Anderson, S. He, Y. Zhao, W. Li, J. Liu, Y. Guo, C. Jozwiak, A. Bostwick, E. Rotenberg, K. Watanabe, T. Taniguchi, T. Cao, D. Xiao, X. Xu, and Y. Chen, Visualizing electronic structure of twisted bilayer $MoTe_2$ in devices, Commun. Phys. **9**, 62 (2026).

[22] K. Kang, Y. Qiu, B. Shen, K. Lee, Z. Xia, Y. Zeng, K. Watanabe, T. Taniguchi, J. Shan, and K. F. Mak, Time-reversal symmetry breaking fractional quantum spin Hall insulator in moiré $MoTe_2$, arXiv:2501.02525.

[23] Y. Wang, G. E. Minarik, W. Li, Y. Kwan, S. Yuan, E. Anderson, C. Hu, J. Ingham, J. Choe, T. Taniguchi, K. Watanabe, X. Roy, J.-H. Chu, R. Queiroz, J. C. Hone, N. Regnault, X. Xu, and X. Zhu, Magnetic signatures of a putative fractional topological insulator in twisted $MoTe_2$ Phys. Rev. X **16**, 031009 (2026).

[24] Z. Sun, F. Xu, J. Li, Y. Jiang, J. Gao, C. Xu, T. Jia, K. Cheng, J. Zhang, W. Tian, K. Watanabe, T. Taniguchi, J. Jia, S. Jiang, Y. Zhang, Y. Zhang, S. Lei, X. Liu, and T. Li, Twist-angle-dependent quantum phase diagrams in twisted bilayer $MoTe_2$, Nature (2026).

[25] E. Tang, J.-W. Mei, and X.-G. Wen, High-temperature fractional quantum Hall states, Phys. Rev. Lett. **106**, 236802 (2011).

[26] K. Sun, Z. Gu, H. Katsura, and S. Das Sarma, Nearly flatbands with nontrivial topology, Phys. Rev. Lett. **106**, 236803 (2011).

[27] T. Neupert, L. Santos, C. Chamon, and C. Mudry, Fractional quantum Hall states at zero magnetic field, Phys. Rev. Lett. **106**, 236804 (2011).

[28] D. N. Sheng, Z.-C. Gu, K. Sun, and L. Sheng, Fractional quantum Hall effect in the absence of Landau levels, Nat. Commun. **2**, 389 (2011).

[29] N. Regnault and B. A. Bernevig, Fractional Chern insulator, Phys. Rev. X **1**, 021014 (2011).

[30] H. Li, U. Kumar, K. Sun, and S.-Z. Lin, Spontaneous fractional Chern insulators in transition metal dichalcogenide moiré superlattices, Phys. Rev. Res. **3**, L032070 (2021).

[31] V. Crépel and L. Fu, Anomalous Hall metal and fractional Chern insulator in twisted transition metal dichalcogenides, Phys. Rev. B **107**, L201109 (2023).

[32] N. Morales-Durán, J. Wang, G. R. Schleder, M. Angeli, Z. Zhu, E. Kaxiras, C. Repellin, and J. Cano, Pressure-enhanced fractional Chern insulators along a magic line in moiré transition metal dichalcogenides, Phys. Rev. Res. **5**, L032022 (2023).

[33] A. P. Reddy, F. Alsallom, Y. Zhang, T. Devakul, and L. Fu, Fractional quantum anomalous Hall states in twisted bilayer $MoTe_2$ and WSe_2, Phys. Rev. B **108**, 085117 (2023).

[34] A. P. Reddy and L. Fu, Toward a global phase diagram of the fractional quantum anomalous Hall effect, Phys. Rev. B **108**, 245159 (2023).

[35] C. Wang, X.-W. Zhang, X. Liu, Y. He, X. Xu, Y. Ran, T. Cao, and D. Xiao, Fractional Chern insulator in twisted bilayer $MoTe_2$, Phys. Rev. Lett. **132**, 036501 (2024).

[36] J. Dong, J. Wang, P. J. Ledwith, A. Vishwanath, and D. E. Parker, Composite Fermi Liquid at Zero Magnetic Field in Twisted $MoTe_2$, Phys. Rev. Lett. **131**, 136502 (2023).

[37] T. Wang and M. P. Zaletel, Chiral superconductivity near a fractional Chern insulator, arXiv:2507.07921.

[38] A. M. Läuchli, Z. Liu, E. J. Bergholtz, and R. Moessner, Hierarchy of fractional Chern insulators and competing compressible states, Phys. Rev. Lett. **111**, 126802 (2013).

[39] A. Abouelkomsan, K. Yang, and E. J. Bergholtz, Quantum metric induced phases in moiré materials, Phys. Rev. Res. **5**, L012015 (2023).

[40] J. Yu, J. Herzog-Arbeitman, M. Wang, O. Vafek, B. A. Bernevig, and N. Regnault, Fractional Chern insulators versus nonmagnetic states in twisted bilayer $MoTe_2$, Phys. Rev. B **109**, 045147 (2024).

[41] A. Abouelkomsan, A. P. Reddy, L. Fu, and E. J. Bergholtz, Band mixing in the quantum anomalous Hall regime of twisted semiconductor bilayers, Phys. Rev. B **109**, L121107 (2024).

[42] C. Xu, J. Li, Y. Xu, Z. Bi, and Y. Zhang, Maximally localized Wannier functions, interaction models, and fractional quantum anomalous Hall effect in twisted bilayer $MoTe_2$, Proc. Natl. Acad. Sci. USA **121**, e2316749121 (2024).

[43] M. Gonçalves, J. F. Mendez-Valderrama, J. Herzog-Arbeitman, J. Yu, X. Xu, D. Xiao, B. A. Bernevig, and N. Regnault, Spinless and spinful charge excitations in moiré fractional Chern insulators, Phys. Rev. Lett. **136**, 196503 (2026).

[44] Y. He, S. H. Simon, and S. A. Parameswaran, Fractional Chern insulators and competing states in a twisted $MoTe_2$ lattice model, arXiv:2505.06354.

[45] X. Li, Y. Chen, B. Li, H. Chen, F. Wu, J. Chen, and W. Ren, Deep learning sheds light on integer and fractional topological insulators, arXiv:2503.11756.

[46] D. Luo, T. Zaklama, and L. Fu, Solving fractional electron states in twisted $MoTe_2$ with deep neural network, arXiv:2503.13585.

[47] R. Hou and A. H. Nevidomskyy, Stabilizing fractional Chern states in twisted $MoTe_2$: Multi-band correlations via non-perturbative renormalization group, arXiv:2511.16641.

[48] N. Morales-Durán, N. Wei, J. Shi, and A. H. MacDonald, Magic angles and fractional Chern insulators in twisted homobilayer transition metal dichalcogenides, Phys. Rev. Lett. **132**, 096602 (2024).

[49] J. Shi, N. Morales-Durán, E. Khalaf, and A. H. MacDonald, Adiabatic approximation and Aharonov-Casher bands in twisted homobilayer transition metal dichalcogenides, Phys. Rev. B **110**, 035130 (2024).

[50] Y. Aharonov and A. Casher, Ground state of a spin-$\frac{1}{2}$ charged particle in a two-dimensional magnetic field, Phys. Rev. A **19**, 2461 (1979).

[51] J. Shi, J. Cano, and N. Morales-Durán, Effects of Berry curvature on ideal fractional Chern insulator many-body gaps, Phys. Rev. Res. **8**, L022045 (2026).

[52] I. Sodemann and A. H. MacDonald, Landau level mixing and the fractional quantum Hall effect, Phys. Rev. B **87**, 245425 (2013).

[53] S. H. Simon and E. H. Rezayi, Landau level mixing in the perturbative limit, Phys. Rev. B **87**, 155426 (2013).

[54] W. Bishara and C. Nayak, Effect of Landau level mixing on the effective interaction between electrons in the fractional quantum Hall regime, Phys. Rev. B **80**, 121302 (2009).

[55] M. R. Peterson and C. Nayak, More realistic Hamiltonians for the fractional quantum Hall regime in GaAs and graphene, Phys. Rev. B **87**, 245129 (2013).

[56] G. Murthy and R. Shankar, Hamiltonian theory of the fractional quantum Hall effect: Effect of Landau level mixing, Phys. Rev. B **65**, 245309 (2002).

[57] E. H. Rezayi, Landau level mixing and the ground state of the $\nu = 5/2$ quantum Hall effect, Phys. Rev. Lett. **119**, 026801 (2017).

[58] A. Wójs, C. Tőke, and J. K. Jain, Landau-level mixing and the emergence of Pfaffian excitations for the 5/2 fractional quantum Hall effect, Phys. Rev. Lett. **105**, 096802 (2010).

[59] D. Yoshioka, Effect of the Landau level mixing on the ground state of two-dimensional electrons, J. Phys. Soc. Jpn. **53**, 3740 (1984).

[60] D. Yoshioka, Excitation energies of the fractional quantum Hall effect, J. Phys. Soc. Jpn. **55**, 885 (1986).

[61] D. Yoshioka, Effect of the higher Landau levels on the excitation spectrum of the ground state of 2D electrons, Surf. Sci. **170**, 125 (1986).

[62] J. Zhao, Y. Zhang, and J. K. Jain, Crystallization in the fractional quantum Hall regime induced by Landau-level mixing, Phys. Rev. Lett. **121**, 116802 (2018).

[63] Z. Papić and D. A. Abanin, Topological phases in the zeroth Landau level of bilayer graphene, Phys. Rev. Lett. **112**, 046602 (2014).

[64] N. D. Le and T. Jolicoeur, Competing Laughlin state and Wigner crystal in Bernal bilayer graphene, Phys. Rev. B **107**, 125129 (2023).

[65] A. Kou, B. E. Feldman, A. J. Levin, B. I. Halperin, K. Watanabe, T. Taniguchi, and A. Yacoby, Electron-hole asymmetric integer and fractional quantum Hall effect in bilayer graphene, Science **345**, 55 (2014).

[66] P. Maher, L. Wang, Y. Gao, C. Forsythe, T. Taniguchi, K. Watanabe, D. Abanin, Z. Papić, P. Cadden-Zimansky, J. Hone, P. Kim, and C. R. Dean, Tunable fractional quantum Hall phases in bilayer graphene, Science **345**, 61 (2014).

[67] D.-K. Ki, V. I. Fal'ko, D. A. Abanin, and A. F. Morpurgo, Observation of even denominator fractional quantum Hall effect in suspended bilayer graphene, Nano Lett. **14**, 2135 (2014).

[68] C. Repellin, T. Neupert, Z. Papić, and N. Regnault, Single-mode approximation for fractional Chern insulators and the fractional quantum Hall effect on the torus, Phys. Rev. B **90**, 045114 (2014).

[69] A. H. MacDonald and D. B. Murray, Broken symmetry states for two-dimensional electrons in a strong magnetic field, Phys. Rev. B **32**, 2291 (1985).

[70] Z. Tešanović, F. Axel, and B. I. Halperin, "Hall crystal" versus Wigner crystal, Phys. Rev. B **39**, 8525 (1989).

[71] Y. Huang, S. Musser, J. Zhu, Y.-Z. Chou, and S. Das Sarma, Apparent inconsistency between Streda formula and Hall conductivity in reentrant integer quantum anomalous Hall effect in twisted $MoTe_2$, Phys. Rev. B **112**, 195136 (2025).

[72] T. Zaklama, D. Luo, and L. Fu, Structure factor and topological bound of twisted bilayer semiconductors at fractional fillings, Phys. Rev. B **112**, L041115 (2025).

[73] A. MacDonald, Influence of Landau-level mixing on the charge-density-wave state of a two-dimensional electron gas in a strong magnetic field, Phys. Rev. B **30**, 4392 (1984).

[74] X. Zhu and S. G. Louie, Wigner crystallization in the fractional quantum Hall regime: A variational quantum Monte Carlo study, Phys. Rev. Lett. **70**, 335 (1993).

[75] Y. Jia, J. Yu, J. Liu, J. Herzog-Arbeitman, Z. Qi, H. Pi, N. Regnault, H. Weng, B. A. Bernevig, and Q. Wu, Moiré fractional Chern insulators. I. First-principles calculations and continuum models of twisted bilayer $MoTe_2$, Phys. Rev. B **109**, 205121 (2024).

[76] N. Morales-Durán, T. M. Wolf, J. Shi, T. Soejima, A. J. Millis, and J. Cano, Non-uniform quantum geometry stabilizes generalized Wigner crystals, arXiv:2609.04149.

[77] J. Zhu, Y. Huang, X. Hu, D. Xiao, and T. Cao, Crystallization in the fractional quantum Hall regime with disorder-aware neural quantum states, arXiv:2604.06316.

[78] X. Hu, D. Xiao, and Y. Ran, Hyperdeterminants and composite fermion states in fractional Chern insulators, Phys. Rev. B **109**, 245125 (2024).

[79] X. Hu, Y. Ran, and D. Xiao, Composite fermion theory of fractional Chern insulator stability, Phys. Rev. Lett. **136**, 066504 (2026).

[80] T. Lu and L. H. Santos, Fractional Chern insulators in twisted bilayer $MoTe_2$: A composite fermion perspective, Phys. Rev. Lett. **133**, 186602 (2024).

[81] T. Lu, Y.-M. Wu, and L. H. Santos, Electromagnetic response and emergent topological orders in transition metal dichalcogenide $MoTe_2$ bilayers, Phys. Rev. B **112**, 085138 (2025).

[82] Topological insulators in twisted transition metal dichalcogenide homobilayers, Phys. Rev. Lett. **122**, 086402 (2019).

[83] C. Repellin, B. A. Bernevig, and N. Regnault, $\mathbb{Z}_2$ fractional topological insulators in two dimensions, Phys. Rev. B **90**, 245401 (2014).

[84] P. Wilhelm, T. C. Lang, and A. M. Läuchli, Interplay of fractional Chern insulator and charge density wave phases in twisted bilayer graphene, Phys. Rev. B **103**, 125406 (2021).

[85] D. Guerci, A. Abouelkomsan, and L. Fu, From fractionalization to chiral topological superconductivity in a flat Chern band, Phys. Rev. Lett. **135**, 186601 (2025).

[86] F. D. M. Haldane, Fractional quantization of the Hall effect: A hierarchy of incompressible quantum fluid states, Phys. Rev. Lett. **51**, 605 (1983).

[87] X. G. Wen and A. Zee, Shift and spin vector: New topological quantum numbers for the Hall fluids, Phys. Rev. Lett. **69**, 953 (1992).

[88] J. Thomson, On the structure of the atom: an investigation of the stability and periods of oscillation of a number of corpuscles arranged at equal intervals around the circumference of a circle; with application of the results to the theory of atomic structure, London, Edinburgh, Dublin Philos. Mag. J. Sci. **7**, 237 (1904).

[89] A. C. Archer, K. Park, and J. K. Jain, Competing crystal phases in the lowest Landau level, Phys. Rev. Lett. **111**, 146804 (2013).